A&A 628, A41 (2019)
https://doi.org/10.1051/0004-6361/201731674

Astronomy & Astrophysics

Activity and rotation of the X-ray emitting *Kepler* stars

D. Pizzocaro[1,2], B. Stelzer[3,4], E. Poretti[5], S. Raetz[3], G. Micela[4], A. Belfiore[1], M. Marelli[1], D. Salvetti[1], and A. De Luca[1,6]

[1] INAF – Istituto di Astrofisica Spaziale e Fisica Cosmica Milano, via E. Bassini 15, 20133 Milano, Italy
e-mail: daniele.pizzocaro@gmail.com
[2] Università degli Studi dell' Insubria, Via Ravasi 2, 21100 Varese, Italy
[3] Institut für Astronomie & Astrophysik, Eberhard-Karls-Universität Tübingen, Sand 1, 72076 Tübingen, Germany
[4] INAF – Osservatorio Astronomico di Palermo, Piazza del Parlamento 1, 90134 Palermo, Italy
[5] INAF – Osservatorio Astronomico di Brera, via E. Bianchi 46, 23807 Merate (LC), Italy
[6] INFN – Istituto Nazionale di Fisica Nucleare, Sezione di Pavia, via A. Bassi 6, 27100 Pavia, Italy

Received 30 July 2017 / Accepted 12 June 2019

ABSTRACT

The relation between magnetic activity and rotation in late-type stars provides fundamental information on stellar dynamos and angular momentum evolution. Rotation-activity studies found in the literature suffer from inhomogeneity in the measurement of activity indexes and rotation periods. We overcome this limitation with a study of the X-ray emitting, late-type main-sequence stars observed by *XMM-Newton* and *Kepler*. We measured rotation periods from photometric variability in *Kepler* light curves. As activity indicators, we adopted the X-ray luminosity, the number frequency of white-light flares, the amplitude of the rotational photometric modulation, and the standard deviation in the *Kepler* light curves. The search for X-ray flares in the light curves provided by the EXTraS (Exploring the X-ray Transient and variable Sky) FP-7 project allows us to identify simultaneous X-ray and white-light flares. A careful selection of the X-ray sources in the *Kepler* field yields 102 main-sequence stars with spectral types from A to M. We find rotation periods for 74 X-ray emitting main-sequence stars, 20 of which do not have period reported in the previous literature. In the X-ray activity-rotation relation, we see evidence for the traditional distinction of a saturated and a correlated part, the latter presenting a continuous decrease in activity towards slower rotators. For the optical activity indicators the transition is abrupt and located at a period of ∼10 d but it can be probed only marginally with this sample, which is biased towards fast rotators due to the X-ray selection. We observe seven bona-fide X-ray flares with evidence for a white-light counterpart in simultaneous *Kepler* data. We derive an X-ray flare frequency of ∼0.15 d^{-1}, consistent with the optical flare frequency obtained from the much longer *Kepler* time-series.

Key words. stars: activity – methods: observational – stars: atmospheres – magnetic fields – X-rays: stars – dynamo

1. Introduction

Main sequence stars are characterized by radiative emission processes, such as high-energy (UV and X-ray) emission, flares, and enhanced optical line emission (Ca II, Hα), collectively referred to as "magnetic activity", as they are ascribed to processes involving magnetic fields in the stellar corona, chromosphere, and photosphere. Magnetic activity is allegedly the result of internal magnetic dynamos, arising from the combination of stellar differential rotation and convection in the sub-photospheric layers.

The understanding of stellar magnetic activity is of capital importance, since it is a fundamental diagnostics for the structure and dynamics of stellar magnetic fields, and gives crucial information on the dynamo mechanism responsible for their existence. Besides this, the high-energy emission associated with magnetic activity has a fundamental role in the evolution of the circumstellar environment and on the composition and habitability of planets.

As stated above, rotation is one of the key ingredients of stellar dynamos. In a feedback mechanism, the coupling of the rotation itself with the magnetic field determines the spin evolution of stars. This is true both in the pre-main-sequence phase (in which the angular momentum of the accretion disk is transferred to the central forming star through the magnetic field) and in the main-sequence phase (because of the momentum loss due to magnetized winds ejected by the star). Exploring the relation between the stellar magnetic activity and the star's rotation rate is thus an efficient way to gather information on stellar dynamos.

The connection between stellar rotation and magnetic activity has been studied in many works, since the seminal papers by Wilson (1966) and Kraft (1967). A fundamental contribution was made through the work by Skumanich (1972), the first to interpret the activity-rotation relation as a consequence of a dynamo mechanism. Since then, many authors (e.g., Walter & Bowyer 1981; Dobson & Radick 1989; Micela et al. 1985; Pizzolato et al. 2003) have focused on the relation between the stellar rotation and specific chromospheric and coronal activity indicators. From these works, a bimodal distribution emerged for the rotation-activity relation: for rotation periods longer than a few days (depending on the spectral type of the star, or the equivalent parameters of stellar mass or color), the activity decreases with the rotation period; for shorter periods, a saturation regime is reached in which the activity level is independent of the rotation period. Since rotation is an ingredient of the dynamo mechanism, a correlation between rotation and activity is intuitively reasonable. The origin of the saturation, instead, has not been ascertained. It may be due to a change in the behaviour of the dynamo, or due to limits to the coronal emission because the stars run out of the available surface to accomodate more active regions (O'dell et al. 1995), or because the high rotation

Table 1. *XMM-Newton* observations from the 3XMM-DR5 Catalog in the *Kepler* FoV.

OBS_ID	RA(J2000)	Dec(J2000)	Obs. date	Exp. time (ks)	$f_{\rm X,lim}$ (erg cm^{-2} s^{-1})
0302150101	19 21 05.99	+43 58 24.0	2005-10-10	16.9	1.46×10^{-14}
0302800101	19 59 28.28	+40 44 02.0	2005-10-14	22.5	3.35×10^{-14}
0302800201	19 59 28.28	+40 44 02.0	2005-10-16	18.8	1.43×10^{-14}
0302150201	19 21 05.99	+43 58 24.0	2005-11-14	16.9	6.27×10^{-15}
0553510201	19 41 17.98	+40 11 12.0	2008-05-18	26.9	2.8×10^{-15}
0551021701	19 41 51.86	+50 31 01.8	2008-11-08	11.7	2.27×10^{-15}
0550451901	19 47 19.42	+44 49 40.8	2008-11-20	17.9	1.16×10^{-14}
0600040101	19 21 11.41	+43 56 56.2	2009-11-29	58.3	8.35×10^{-15}
0653190201	20 01 40.00	+43 52 20.0	2010-06-23	15.9	4.02×10^{-14}
0670140501	19 36 59.90	+46 06 28.0	2011-05-10	31.9	2.44×10^{-15}
0672530301	19 05 25.90	+42 27 40.0	2011-06-05	29.1	1.93×10^{-15}
0671230401	19 58 00.01	+44 40 00.0	2011-06-09	85.9	2.53×10^{-15}
0671230301	19 58 00.01	+45 10 00.0	2011-06-23	83.9	3.37×10^{-15}
0671230101	19 55 59.98	+44 40 00.0	2011-09-25	81.9	2.53×10^{-15}
0671230201	19 55 59.98	+45 10 00.0	2012-03-26	104.5	1.84×10^{-15}
0671230601	19 55 59.98	+45 10 00.0	2012-03-26	2.7	1.10×10^{-13}

Notes. Next to observation ID (Col. 1), pointing center (Cols. 2 and 3), observing date (Col. 4) and exposure time (Col. 5), the flux sensitivity limit is given (Col. 6) calculated as described in Sect. 2.2.

rate causes centrifugal stripping of the stellar corona (Jardine & Unruh 1999).

X-ray emission is a very good proxy for stellar activity: the X-ray activity of a star is the result of magnetic reconnection in the stellar corona, an abrupt change in the configuration of the magnetic field determining the release of nonpotential energy stored in the magnetic field lines. Rotation-activity studies found in the literature typically refer to collections of X-ray data obtained from various instruments, and rotation periods measured with different techniques, combining ground-based photometric measurments with $v \sin i$ spectroscopic techniques. The limitations due to the use of inhomogeneous datasets can now be overcome by combining rotation periods from the *Kepler* optical light curves to X-ray data obtained with *XMM-Newton*, which has observed ∼1500 objects in the *Kepler* field of view.

In the present work we study the relationship between the rotational properties and the magnetic activity of the X-ray emitting main-sequence field stars observed with the *Kepler* mission. We compare various indicators for activity (X-ray and UV activity, white-light flaring rate, flare amplitude, *Kepler* light curve amplitude, and standard deviation) and rotation (rotation period and Rossby number; Noyes et al. 1984).

The sample selection is described in Sect. 2. The procedure used to evaluate the physical parameters of all stars in the sample is described in Sect. 3. In Sect. 4 we describe the techniques used to determine the rotation period and photometric activity diagnostics. In Sect. 5, several indicators of stellar activity are analyzed: the X-ray luminosity, the ultraviolet excess in the spectral energy distribution (SED), the white-light and X-ray flaring activity. The results are discussed in Sect. 6 and conclusions are presented in Sect. 7.

2. Sample selection

A proper sample selection is crucial in order to obtain a reliable picture of the activity-rotation relation. Many rotation-activity studies have been performed on inhomogeneous samples of stars for which X-ray data had been collected from a set of various databases and using a combination of spectroscopic and photometric techniques for rotation measurements.

We aim to the highest homogeneity in the determination of the rotation period and in the characterization of the activity indicators, first of all the X-ray activity. To this end, we focused in this work on X-ray emitting stars detected by *XMM-Newton* with light curves from *Kepler*. We performed a positional match between the 3XMM-DR5 catalog (Rosen et al. 2016) and the *Kepler* Input Catalog (KIC, Brown et al. 2011), and then removed nonstellar objects and objects with uncertain photometry.

The 3XMM-DR5 catalog includes data from 16 *XMM-Newton* pointings within the field of view (FoV) of the *Kepler* mission (see Table 1). Their sky position is shown in Fig. 1. The *Kepler* FoV covers ∼105 square degrees; the 16 *XMM-Newton* observations that fall inside this FoV cover only ∼2% of that area.

The KIC positional error (∼0.1″) is negligible with respect to the error in the 3XMM-DR5 position ($\lesssim$4″ at 3σ). We selected all the 3XMM-DR5 unique[1] sources that have a positional match (columns SC_RA, SC_DEC in 3XMM-DR5) with one or more KIC objects within a radius given by three times their 3XMM-DR5 individual (1σ) positional error (column SC_POSERR). We calculated the average probability of a chance association between a 3XMM-DR5 source and a KIC source in each *XMM-Newton* field as $P = 1 - e^{-\pi\mu r^2}$, where μ is the numerical density of KIC sources in the field and has a typical value of 10^{-4} sources arcsec^{-2}, and r is three times the average position error of the 3XMM-DR5 source. We obtained an average probability of chance association of ∼0.8%. This translates to ∼0.14 chance associations per *XMM-Newton* field, meaning ∼2 spurious matches in the whole sample.

We selected only the objects with a detection significance in 3XMM-DR5 (column DET_ML) greater than 6 (probability of a spurious detection <0.025) in at least one EPIC instrument in

[1] The 3XMM-DR5 Catalog contains a row for each X-ray detection. For a certain "unique" source (the astrophysical object), many detections (referring to different observations) of that object may be available.

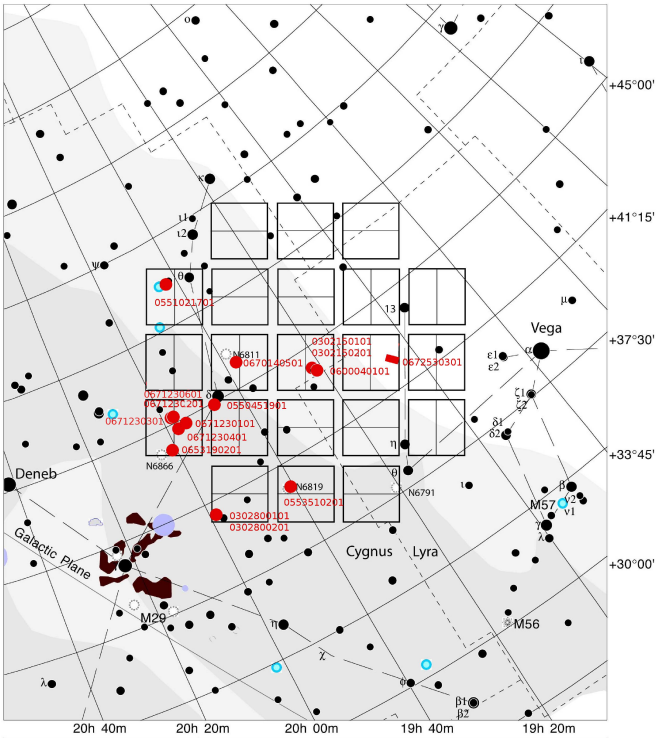

Fig. 1. Field of view (FoV) of the *Kepler* mission is respresented by the solid black squares. It is centered at RA = 19° 22 40.0 , Dec = +44° 30 00.0, between the Cygnus and the Lyra constellation. The FoVs of the sixteen 3XMM-DR5 observations we analyzed (Table 1) are reported as red circles; the red numbers represent the 3XMM-DR5 unique observation ID (OBS_ID). The FoVs of some *XMM-Newton* observations are totally or partially overlapping.

the energy band 8 (0.2−12.0 keV), removing the others from the sample (4 objects removed). We rejected the 21 sources that were classified as "extended" in 3XMM-DR5 (flag EP_EXTENT > 6). The resulting sample consists of 145 matches. There are no multiple associations, that is associations between a KIC object and two or more 3XMM-DR5 objects, or viceversa.

Within this sample, we aimed to identify genuine stars, removing (1) galaxies and (2) stars that possibly suffer confusion (stars which are not resolved by *Kepler*) and contamination from nearby bright sources. To this end, for each KIC object with a 3XMM-DR5 match, we searched for a classification in the SIMBAD database[2] (Wenger et al. 2000) and we inspected the optical and infrared images, when available, using the Aladin service (Bonnarel et al. 2000; Boch & Fernique 2014). The fit of the spectral energy distribution (SED) with a model for the stellar photospheric emission is also useful to identify galaxies in the sample (objects whose SED cannot be fit by a stellar model). Moreover, it allows us to determine the value of the stellar fundamental parameters. The methods to remove nonstellar counterparts to the X-ray sources are explained in more detail in the following.

2.1. Spectral energy distribution (SED)

2.1.1. Multiwavelength photometry

We extracted the IR (2MASS J, H, K), optical (SLOAN g, r, i, z, Johnson U, B, V, *Kepler* K_p) and UV (GALEX FUV, NUV) photometry for all stars of our sample from the KIC (Brown et al. 2011). Many sources lack photometry in one or more of these bands. We excluded from the sample the KIC objects for which no 2MASS IR photometry was available (2 objects), since the wavelength range covered by 2MASS is crucial in order to perform a reliable spectral classification.

The visual inspection of the optical images via the Aladin server indicated that some stars suffer contamination from brighter objects located nearby. In such cases, even if they are recognized as distinct objects in the KIC, the photometry of the fainter one is expected to be significantly contaminated by the brighter one. Other stars suffer confusion between unresolved objects, which means that they are not resolved in the KIC survey, but can be recognized as two objects through visual inspection of the optical image. When the object was resolved in the UCAC-4 Catalog (Zacharias et al. 2012), we replaced the KIC photometry for these confused objects with the photometry provided by UCAC-4 for the brightest one. If no UCAC-4 photometry was available, we removed the object from our sample (2 objects).

According to Pinsonneault et al. (2012), the SLOAN bands photometry reported in the KIC present a significant systematic error, as observed comparing the KIC photometry in the bands g, r, i, z with the photometry reported in the Sloan Digital Sky Survey (SDSS-DR8) in the same bands, available for ∼10% of the full KIC. Pinsonneault et al. (2012) give semi-empirical formulas to correct these systematics (their Eqs. (1)–(4)). We applied these corrections to the KIC SLOAN bands photometry of all the stars of our sample. The photometry for all the stars in our sample is reported in Table A.1.

2.1.2. SED fitting

After compiling the SEDs, we fit them with photospheric BT-Settl models (Allard et al. 2012) within the Virtual Observatory SED Analyzer (VOSA, Bayo et al. 2008). The parameters of the BT-Settl models are: A_V, $\log g$, [Fe/H], and $T_{\rm eff}$. Due to parameter degeneracy it is not possible to determine all of them from the SED fit. Therefore we adopted for each star for A_V, $\log g$, and [Fe/H] values taken from the literature (see Sect. 3), leaving $T_{\rm eff}$ as the only free parameter. We thus obtained, for each object, a best fit $T_{\rm eff}$ under the hypothesis of a stellar model. As the uncertainty on the effective temperature we assumed the typical dispersion of the five best fit values obtained in VOSA for each object (±200 K).

From the shape of their SED, combined with the visual inspection of the Aladin images, 16 objects were recognized as galaxies, and we removed them from our sample. The whole sample selection procedure eventually results in a sample of 125 3XMM-DR5 unique sources with a reliable stellar counterpart in *Kepler*, with a SED that is well-fitted by a stellar photosphere model.

2.2. X-ray flux limit

The sample of stars used in the present work has been selected based on the X-ray emission observed by *XMM-Newton* and as such is biased towards X-ray active stars. A fundamental step in order to understand the results presented in this work is, therefore, to provide an evaluation of the X-ray flux limit of the sample. To this end, we first produced the EPIC PN[3] sensitivity map for each *XMM-Newton* observation of Table 1, for the

[2] http://simbad.u-strasbg.fr/simbad/

[3] The EPIC (European Photon Imaging Camera) consists of three CCD detectors, two MOS and one PN, located at the focus of the three grazing incidence multi-mirror X-ray telescopes which constitute the main instrument onboard *XMM-Newton*.

energy range 0.2−2.0 keV using the task `esensmap` of the *XMM-Newton* Science Analysis Software (SAS). The sensitivity map provides in each point of the FoV the limiting count rate needed to have a 3σ detection of a point source. We measured the limiting count rate in the center of the FoV. We converted these numbers into flux sensitivity limits ($f_{\rm X,lim}$) using WebPIMMS[4] assuming an APEC model with plasma temperature 0.86 keV (see Sect. 5.1.2), abundance 0.2 in solar units, and the galactic hydrogen column density provided by Kalberla et al. (2005). The resulting numbers for $f_{\rm X,lim}$ are reported in the last column of Table 1. These values give an idea of the lower limit for the X-ray flux in these observations (median is $\sim 6 \times 10^{-15}$ erg cm^{-2} s^{-1}), although we caution that the sensitivity varies strongly (up to about one order of magnitude) from the center to the outer region of the FoV.

3. Fundamental stellar parameters

3.1. Effective temperature, visual absorption, surface gravity, and metallicity

For 119 stars out of 125 we found literature values for effective temperature ($T_{\rm eff}$), visual absorption ($A_{\rm V}$) surface gravity ($\log g$), and metallicity ([Fe/H]) (in Huber et al. 2014 and Frasca et al. 2016). Huber et al. (2014) present a compilation of literature values for atmospheric properties ($T_{\rm eff}$, $\log g$ and [Fe/H]) derived from different observational techniques (photometry, spectroscopy, asteroseismology, and exoplanet transits), which were then homogeneously fitted to a grid of isochrones from the Dartmouth Stellar Evolution Program (DSEP; Dotter et al. 2008), for a set of ∼200 000 stars observed by the *Kepler* mission in Quarters 1−16. Frasca et al. (2016) present a systematic spectroscopic study of ∼50 000 *Kepler* stars performed using the LAMOST telescope (Zhao et al. 2012). We compared the parameters obtained by Huber et al. (2014) and Frasca et al. (2016) for our sample, in particular the effective temperatures, and we found that they agree very well within the error bars. When available, however, we preferred the values obtained from Frasca et al. (2016) through the spectroscopic analysis, since in that work the stellar parameters have been evaluated using the same method for all the stars in their sample, while Huber et al. (2014) present a collection of values obtained in several works using different techniques.

Six stars in the sample do not have $T_{\rm eff}$ reported in Huber et al. (2014) or Frasca et al. (2016). For these 6 stars we adopted as $T_{\rm eff}$ the effective temperature of the best fit of the individual SED with a model of the stellar photosphere, as described in Sect. 2.1. These stars are flagged with the "VOSA" flag in Col. 12 of Table A.2. Two out of these 6 stars have values for $A_{\rm V}$, [Fe/H] and $\log g$ in Huber et al. (2014) or Frasca et al. (2016), and we used them in the SED fit. For the others, we adopted the median values of the distribution of $A_{\rm V}$ in our sample (0.38), $[{\rm Fe/H}]_\odot$ (0.0) and $\log g$ (4.0). Similarly, for the additional 15 stars that have no literature value for $A_{\rm V}$ we adopted the median of 0.38 mag. The adopted values for the spectral parameters of all 125 stars are listed in Table A.2.

In order to validate our SED fitting procedure we compared the obtained $T_{\rm eff}$ with the ones from the above-mentioned literature sources. The distribution of $T_{\rm eff}$ and the comparison between the $T_{\rm eff}$ obtained from the SED fitting and the values in the literature are reported in Fig. 2. Within the error bars, the agreement is for most stars very good, but the error bars of the values obtained by SED fitting are typically larger than the error bars in Huber et al. (2014) and especially in Frasca et al. (2016). This justifies our decision to adopt, when available, the literature values for $T_{\rm eff}$. Given the effective temperature, we assigned a spectral type to each star according to Table 5 in Pecaut & Mamajek (2013). These values are given in Table A.2.

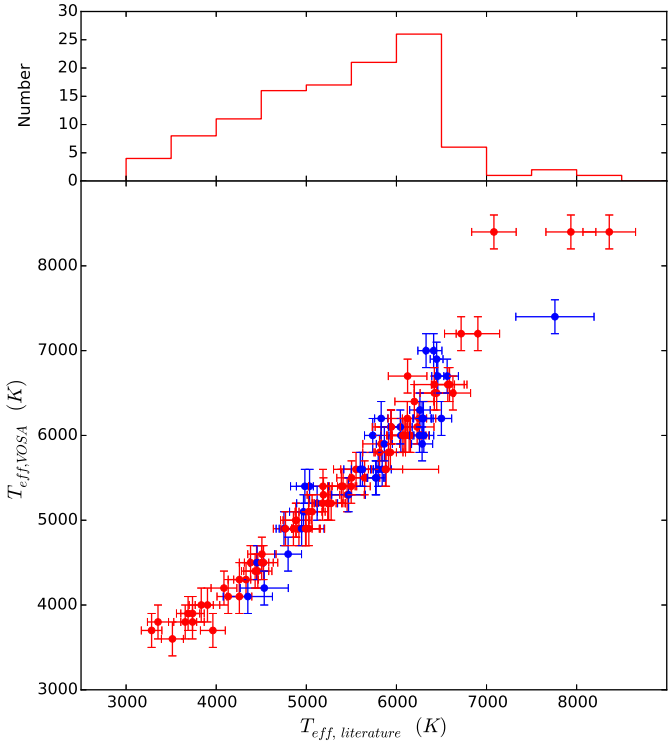

Fig. 2. *Upper panel*: distribution of the $T_{\rm eff}$ of the 119 stars in our sample with $T_{\rm eff}$ taken from the literature (Huber et al. 2014; Frasca et al. 2016). *Lower panel*: comparison between the $T_{\rm eff}$ drawn from the literature and the ones obtained with the SED fitting is reported for the same sample of stars. The colors represent the original work in which the $T_{\rm eff}$ was derived. Blue: Frasca et al. (2016); red: Huber et al. (2014).

3.2. Distance, mass, and bolometric luminosity

Figure 3 shows our stellar sample together with the DSEP isochrones on the $\log g$ vs. $\log T_{\rm eff}$ plane. For each star, we estimated absolute J band magnitude, mass (M) and bolometric luminosity ($L_{\rm bol}$) by projecting its position and the related uncertainties onto the isochrones (along the vertical axis) in Fig. 3. For this task we made use of DSEP isochrones in the range of 1.0–9.5 Gyr and for each star, we selectdcd the set of isochrones corresponding to the [Fe/H] value closest to the observed value. There are a few stars the position of which on the $\log g$ vs. $\log T_{\rm eff}$ plane is not consistent, within the error bars, with any of the DSEP isochrones. We mark them with a flag ("DSEP outlier") in Table A.2.

Inverting the parallaxes provided in the *Gaia*-DR2 (Gaia Collaboration 2018) we obtain the distances to our targets. While the overall quality of the *Gaia*-DR2 data is excellent, the mission is too complex to achieve optimal calibrations with less than two years of observations. As a result the *Gaia*-DR2 still contains many spurious astrometric solutions (Arenou et al. 2018). To remove putative problematic solutions we cleaned our dataset using the filters defined by Lindegren et al. (2018, Appendix C, Eqs. (C-1) and (C-2)). Furthermore

[4] http://heasarc.gsfc.nasa.gov/cgi-bin/Tools/w3pimms/w3pimms.pl

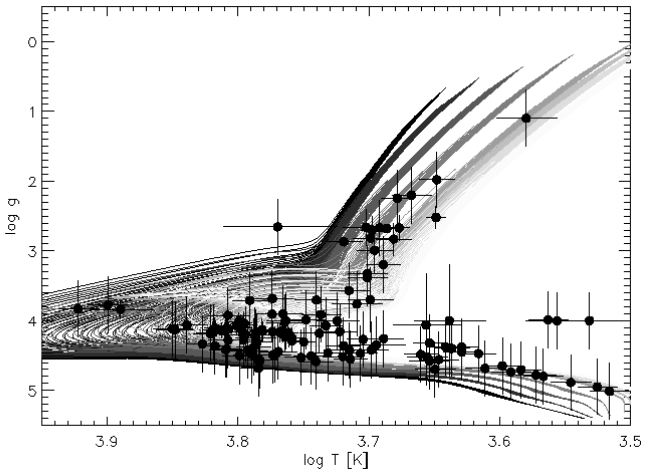

Fig. 3. $\log g - \log T_{\rm eff}$ space with the set of isochrones from DSEP and the stars of our sample (black circles) overplotted. Each stack of isochrones (lines in different gray-shades) corresponds to a given value of [Fe/H] (−2.0, −1.5, −1.0, −0.5, 0.0, 0.2, 0.3, 0.5 from dark to pale).

we used additional quality indicators of the solutions (astrometric_excess_noise > 0, astrometric_gof_al > 5) to discard other potential outliers. Two stars of our sample have no *Gaia* parallax while the solutions for further 60 stars might not be reliable and were filtered out. For these 62 targets we derived the photometric distance from the comparison between the absolute magnitude and the observed J band magnitude. Comparison of the photometric and astrometric distances for the whole sample shows overall good agreement. For 5 targets with reliable *Gaia* distances we found the J band distances to have lower uncertainties. In these cases we decided to adopt the J band distances. To summarize, throughout this work we used the *Gaia* distances for 58 stars and the photometric J band distance for the remaining stars. Distance, mass and bolometric luminosity are reported for all 125 stars in Table A.2.

We classified the stars in our sample as main-sequence stars or giant stars according to their $\log g$. In the $\log g$ vs. $\log T_{\rm eff}$ space, the stars in our sample can be separated into two groups, corresponding to the dwarf branch and to the giant branch, respectively (see Fig. 3). On this basis, we considered as main-sequence stars all the stars with $\log g \geq 3.5$, and as giants all the stars with $\log g < 3.5$. With this criterion we found 19 giant stars. The four stars without $\log g$ value in the literature can not be assigned to these groups; we removed them from the sample. These stars have a flag (*) in Col. 12 of Table A.2. This work is focused on main-sequence stars. Therefore, in the following, if not differently declared, we consider only the sample of the 102 main-sequence stars. The distribution of their adopted distances is plotted in Fig. 4.

4. Analysis of *Kepler* light curves

The brightness modulation in the optical light curve due to the presence of inequally distributed spots on the rotating stellar surface enables the measurement of the stellar rotation period. Rotation periods, together with several photometric activity diagnostics, have been extracted from the *Kepler* light curves following the procedure described by Stelzer et al. (2016). The methods developed therein for the analysis of M dwarf K2 mission lightcurves can readily be applied to the data from the main *Kepler* mission, and we briefly resume the steps in Sect. 4.1.

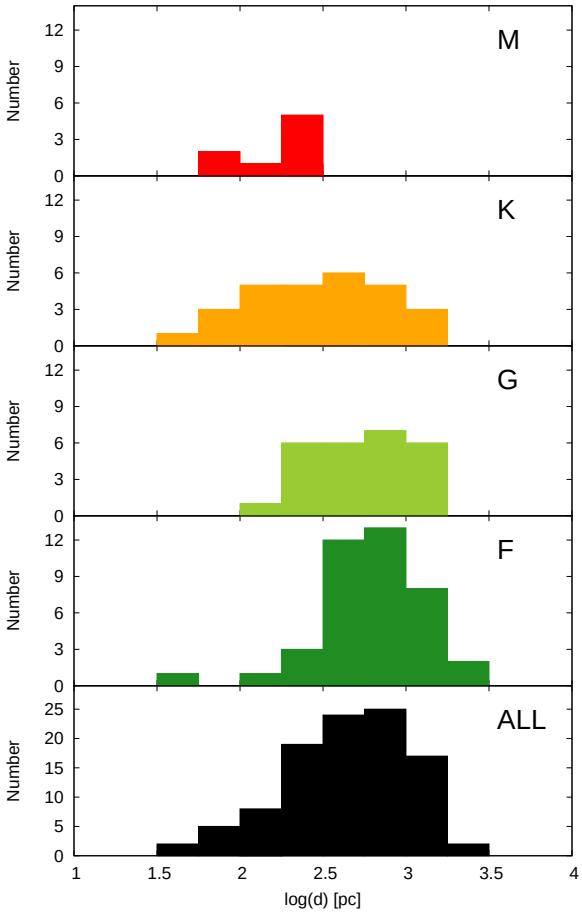

Fig. 4. Distribution of the adopted distances for the individual spectral types (*from top to bottom*: M, K, G, F) and for the whole sample of the main-sequence stars (*bottom panel*).

To obtain a clean sample of stars for the rotation-activity study, periods originating from mechanisms different from the rotational brightness modulation due to starspots must be identified and removed. In particular, our sample covers a broad range of $T_{\rm eff}$ in the Hertzsprung–Russell diagram, including the intersection of the main-sequence with the classical instability strip, where stellar pulsations are expected. Therefore, the light curves of some stars deserve a more detailed study in order to ascertain if pulsation (but also binarity) could be the real cause of the observed variability. We performed this study by means of the Fourier decomposition (Poretti 1994) and the iterative analysis of the whole frequency spectrum (Vaníček 1971), described in Sect. 4.2.

4.1. Search for rotational periodicity

Briefly, the analysis consists of the following steps, implemented in an iterative procedure, which is described in detail by Stelzer et al. (2016): (1) period search with standard time-series analysis techniques (autocorrelation function [ACF] and Lomb–Scargle [LS] periodogram), (2) boxcar smoothing of the lightcurve and subsequent subtraction of the smoothed from the observed lightcurve, effectively removing the rotational modulation, (3) identification of "outlier" data points in the "flattened" lightcurve obtained from step (2) through σ-clipping. The outliers comprise both instrumental artefacts and flares. The latter ones are identified by imposing three criteria: (i) a threshold (3σ) for the significance of the flare data points above the flattened

Table 2. Classification of the main-sequence stars in our sample according to the type of variability observed in the *Kepler* light curves.

SpT	Main sequence (MS) stars	With rotation period	No. period	Ecl. binaries	Other binaries	Pulsators	Unclear
All	102	74	2	10	5	3	3
A	3	2	0	0	0	1	0
F	37	24	2	5	2	1	1
G	26	19	0	1	0	1	1
K	28	21	0	4	3	0	0
M	8	8	0	0	0	0	1

curve, (ii) criterion (i) applies to at least two consecutive such data points, and (iii) the maximum bin of the flare has at least a factor two higher flux than the last bin defining the flare. For a detailed description of the procedure used in each step of the analysis chain see Stelzer et al. (2016).

After the removal of the outliers we repeated the period search, but in practice the applied methods are so robust that the cleaning of the lightcurves did not alter the result. What did change after the cleaning is the amplitude of the rotation cycle, when measured between maximum and minimum flux bin. However, as we describe below in Sect. 4.4, the preferred characterization of the spot cycle amplitude involves diagnostics that are little affected by the small fraction of outlier data points. We performed this analysis for each *Kepler* observing Quarter independently. This allowed us to cross-check the results by comparing the periods obtained from different Quarters, as explained in Sect. 4.3.

The determination of the rotation period for a given star proceeded in the following way. We usede the routines A_CORRELATE and SCARGLE in the IDL environment[5] to generate the ACF and LS periodogram. We worked independently on the ACF and LS periodogram series. For each *Kepler* observing Quarter, we inspected visually the ACF and LS periodogram generated by our procedure, and searched for a signal of periodic variability (a sharp peak at a certain frequency, possibly followed by the related harmonics). If absent, we rejected the Quarter from the analysis. In the ACF periodogram, we visually chose the highest peak of the series, which corresponds to the period of the modulation; this is generally the first one, or the second one if the light curve shows a double-humped pattern (as described below). In the LS periodogram, we likewise chose the highest peak.

For the majority of stars, the dominating periods derived with both techniques (ACF and LS) are consistent with each other. Deviations regard lightcurves with a double-humped shape. In this case, the light curve shows a double peak in at least some of the *Kepler* observing Quarters, while in others a single peak pattern may be observed. We interpret these features as the signature of two groups of spots at a roughly antipodal position on the photosphere of the star, one of which may occasionally disappear. In this case, the ACF periodogram shows generally a first peak (corresponding to half the period) that has a lower amplitude with respect to the second one, and this pattern repeats for the peaks corresponding to integer multiples of the first-peak period and of the second-peak period, respectively. In the Lomb–Scargle periodogram, the peak corresponding to the shorter period often has a larger amplitude than the longer-period peak. The interpretation of these patterns as the effect of two groups of spots on the photosphere allows us to interpret the longer period of the two, corresponding to the double of the other, as the true rotation period of the star.

We obtained for each star N_Q periods, where N_Q is the number of Quarters in which the star shows a periodic signal. This number varies individually for the stars of our sample, independently for the ACF and the LS method. We adopted as the star's period the median value of the periods obtained with the ACF method from the individual quarters.

4.2. Nonrotational periodicity

For some of the stars in our sample periodic variability is identified that can not be explained with a simple spot pattern. In such cases the Fourier decomposition and the evaluation of the whole frequency spectra were very helpful. The frequency spectra of the genuine spotted stars are characterized by the harmonics of the rotational period and by low-frequency peaks due to the activity and rotational cycle-to-cycle period variations due to the shift in the spots' latitude and to stellar differential rotation, and by some rotational cycle-to-cycle variation in the shape and amplitude of the lightcurve due to the variation of the area and shape of starspots. Other kinds of periodicity present different patterns.

We performed a dedicated anlysis of the light curves of the stars that do not show a clear variability pattern in order to classify their nonrotational variability. We found one multiperiodic star showing the high-frequency pulsational regime of δ Sct stars and three multiperiodic stars showing the low-frequency regime of γ Dor stars. In the light curves of two stars the amplitudes of the even Fourier harmonics are much larger than those of the odd ones, as necessary to fit both the sharp minima and the large maxima shown by contact binaries. For three stars it remains ambiguous if the variability is due to star spots or due to orbital motion in a contact binary; another two stars display non-periodic variability that we could not classify. Finally, five stars are likely rotational variables but displaying more than one period possibly indicating a binary composed of two spotted stars or a complex pattern with uncertain period. We removed these 16 stars from the sample considered for the rotation-activity relation. A summary of the number of main-sequence stars in each variability class for spectral type is given in Table 2.

4.3. Final sample of spotted stars

From the analysis described above, we can derive a rotation period for 74 stars in our sample, meaning that these stars are inhomogeneously spotted. For the subsequent analysis, we also computed the Rossby number, defined as $R_0 = P_{\rm rot}/\tau_{\rm conv}$, that is the ratio between the rotation period and the convective turnover time. The convective turnover time is the characteristic

[5] IDL is a product of the Exelis Visual Information Solutions, Inc.

time of circulation within a convective cell in the stellar subphotosphere, and not directly observable. We calculated it from $T_{\rm eff}$ using Eq. (36) in Cranmer & Saar (2011), which is valid in the range $3300\,{\rm K} \lesssim T_{\rm eff} \lesssim 7000\,{\rm K}$. All but two of the stars in our sample are within this range of $T_{\rm eff}$. The rotation periods and Rossby numbers for all "spotted" stars are listed in Table A.3. Our subsequent photometric variability analysis is limited to this sample.

4.4. Photometric activity diagnostics

From the analysis of the *Kepler* light curves we also obtained various diagnostics for the stellar photospheric activity: the light curve amplitude and the standard deviation of the light curve. The light curve amplitude is the photometric difference between the maximum and the minimum of the rotationally-modulated light curve, determined (in a light curve cleaned from flares) by the contrast between spotted and unspotted photosphere, combined with the inhomogeneous distribution of spots which causes the spot coverage of the observed stellar hemisphere to vary during the rotation. Analogous to Stelzer et al. (2016) and for consistency with the previous literature we decided to define the spot cycle amplitude as the range between the 5th and 95th percentile of the observed flux values in a single rotation cycle ($R_{\rm var}$, see Basri et al. 2013), and we adopt the modified definition of $R_{\rm var}$ introduced by McQuillan et al. (2013), $R_{\rm per}$, which is the mean of the $R_{\rm var}$ values measured individually on all observed rotation cycles, expressed in percent. Cutting the upper- and lower-most 5% of the data points is another way of removing the outliers, such that no difference between the $R_{\rm var}$ values obtained from the original light curve with the 5th and 95th percentile and from the cleaned lightcurve is expected. We verified this by comparing the $R_{\rm var}$ values extracted from the light curves cleaned from flares and outliers and the $R_{\rm var}$ values obtained from the original light curves.

The second activity diagnostic extracted from *Kepler* light curves that we use to characterize the variability during the spot cycle is the standard deviation of the whole light curve ($S_{\rm ph}$), and the average of the standard deviations computed for time intervals $k \times P_{\rm rot}$, with k integer, first defined by Mathur et al. (2014a). Mathur et al. (2014a) have shown for a sample of 22 stars that roughly after five rotation cycles the full range of flux variation is reached. Therefore, we computed $S_{\rm ph}$ and $\langle S_{\rm ph,k=5} \rangle$ for the stars in our sample. The standard deviation of the light curve is used as a proxy of magnetic activity also by He et al. (2015), in a study on the activity of two solar-like *Kepler* stars.

Finally, we computed the standard deviation of the flattened light curves ($S_{\rm flat}$), measured on the light curves cleaned from flares and outliers, and from which the rotational cycle has been removed (see description at the beginning of this section). Stelzer et al. (2016) have established this parameter as an indicator for low-level unresolved astrophysical variability such as small unresolved flares and/or small and fast-changing spots for their sample of nearby M dwarfs observed in the K2 mission.

All these photometric activity diagnostics are listed in Table A.3. It is worth noting here that the noise level in the flattened lightcurve is expected to depend on the brightness of the star. In fact, Fig. 5 shows a correlation between the *Kepler* magnitude and $S_{\rm flat}$. As can be seen in Fig. 5, the apparent brightness of our sample stars is on average larger for earlier spectral types. As a consequence, the noise tends to be smaller in those stars. This must be taken into account in the analysis of other kinds of variability; see e.g. Sect. 6.3.

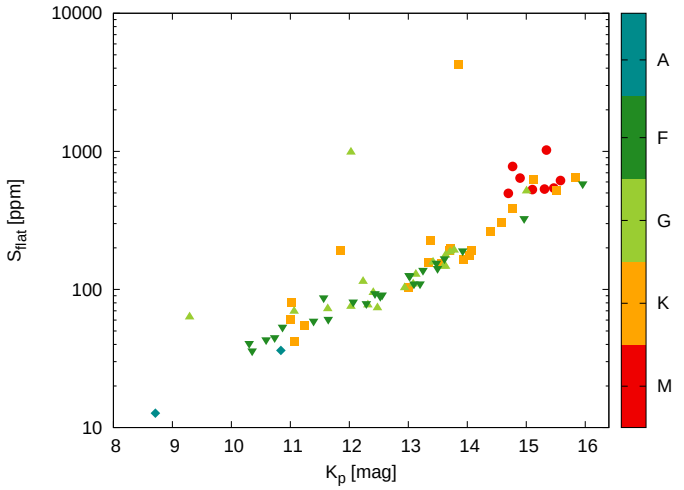

Fig. 5. Standard deviation of the flattened lightcurve ($S_{\rm flat}$) vs. *Kepler* magnitude. Shown is for each star the minimum of $S_{\rm flat}$ from all quarters of observation.

5. X-ray and UV activity

As our sample is X-ray selected, every star in the sample has an associated X-ray detection. In the main-sequence sample, 36 stars have also been detected in one or both of the UV energy bands (Near Ultra-Violet, NUV, and Far Ultra-Violet, FUV) of GALEX. In this section we analyze the X-ray and UV luminosity, and the corresponding activity indexes, defined as the ratio between the luminosity in the high-energy band and the bolometric luminosity of the star, as indicators of the stellar magnetic activity.

5.1. X-ray data analysis

5.1.1. Source X-ray luminosity

We calculated the X-ray luminosity of each star in the sample in the energy band 0.2–2.0 keV ("soft" energy band, 3XMM-DR5 catalog energy band 6). This range of energies corresponds approximately to the energy bands used in previous studies of the rotation-activity connection that were mainly based upon *ROSAT* data (e.g., Wright et al. 2011).

In the 3XMM-DR5 catalog, there are many objects ("sources") that have been observed more than once: so, for a certain source, there can be many detections. Each row of the catalog – which represents an individual detection of a certain source – contains a set of parameters referred to the detection itself, and a set of parameters averaged on all the detections available for that source. The catalog provides the fluxes expected for a power law emission model for both the detections and the source. However, the power law model, to which the fluxes given in 3XMM-DR5 refer, is not appropriate for describing the X-ray emission of late-type stars. Therefore, we re-calculated the X-ray flux in the bands 0.2–2.0 keV from the EPIC PN count rate (or the MOS, if PN is not available), using the HEASARC online tool WebPIMMS, in which we assume for the X-ray emission of the stars a thermal APEC model (Smith et al. 2001). 3XMM-DR5 gives the detection count rate for each of the three EPIC (European Photon Imaging Camera) instruments (PN, MOS1 and MOS2) on board the *XMM-Newton* mission, and the associated uncertainty, but it does not give the source count rate. As described above, the detection count rate is different from the source count rate when the source has multiple detections in

Table 3. Best fit spectral parameters for the 17 brightest X-ray sources (more than 200 counts) identified as rotational variables; parameters are for a `phabs*apec` or `phabs*(apec+apec)` model.

KIC_ID	SpT [a]	Counts [b]	Model	N_H (cm^{-2})	kT (keV)	EM (cm^{-3})
5 112 508	M	520	`Phabs*apec`	~0	0.83	1.31×10^{52}
5 113 557	F	2088	`Phabs*apec`	1.46×10^{20}	0.60	6.40×10^{50}
5 653 243	K	316	`Phabs*apec`	~0	0.80	5.86×10^{52}
6 761 532	G	226	`Phabs*apec`	3.60×10^{20}	0.63	2.43×10^{52}
7 018 708	G	2637	`Phabs*(apec+apec)`	6.80×10^{20}	0.29, 1.04	1.93×10^{53}, 2.24×10^{53}
8 454 353	M	1291	`Phabs*apec`	~0	0.99	9.69×10^{51}
8 517 303	K	1763	`Phabs*apec`	9.10×10^{20}	1.06	1.10×10^{54}
8 518 250	K	434	`Phabs*(apec+apec)`	~0	0.94, 0.23	1.24×10^{51}, 1.88×10^{51}
8 520 065	F	764	`Phabs*(apec+apec)`	2.33×10^{20}	1.07, 0.54	4.30×10^{53}, 3.42×10^{53}
8 584 672	K	230	`Phabs*apec`	~0	0.83	1.21×10^{53}
8 647 865	F	433	`Phabs*apec`	~0	0.49	1.60×10^{52}
8 713 822	K	675	`Phabs*apec`	1.43×10^{20}	1.05	2.58×10^{54}
8 842 083	K	590	`Phabs*apec`	1.1×10^{21}	0.76	7.01×10^{50}
9 048 551	K	1634	`Phabs*apec`	~0	1.07	8.91×10^{51}
9 048 949	K	844	`Phabs*apec`	~0	0.94	4.31×10^{51}
9 048 976	K	285	`Phabs*apec`	~0	0.96	4.11×10^{51}
11 971 335	G	696	`Phabs*apec`	~0	1.30	2.10×10^{53}

Notes. [a] Spectral type has been evaluated from the $T_{\rm eff}$ according to Pecaut & Mamajek (2013). [b]This is the sum of the counts in the three EPIC instruments.

the catalog. This happens for 11 sources in our sample. So, we calculated the X-ray flux for these objects rescaling one of the individual detection count rate for the factor

$$f = \frac{SC\_FLUX_{0.2-2.0}}{DET\_FLUX_{0.2-2.0}} \quad (1)$$

where $SC\_FLUX_{0.2-2.0}$ and $DET\_FLUX_{0.2-2.0}$ are respectively the "source" and "detection" flux provided by 3XMM-DR5.

The APEC model in WebPIMMS requires as input parameters the hydrogen column density (N_H), the metallicity and the temperature of the emitting plasma. We estimated the hydrogen column density for each source from the visual absorption A_V following Cardelli et al. (1989), as

$$N_H = A_V\,(\rm mag) \times 1.79 \times 10^{21}\ cm^{-2}. \quad (2)$$

We adopted an average abundance of 0.2 in solar units, which is a typical value for the coronae of X-ray emitting late-type stars (see e.g. Pandey & Singh 2012). We calculated the count-to-flux conversion factor with WebPIMMS. To establish an operational kT, we fit the spectra of the brightest X-ray sources in XSPEC, and assumed for all stars the kT value in the WebPIMMS grid (kT = 0.86 keV) which is closest to the average kT obtained from the spectral fits (kT = 0.83 keV). The spectral analysis of the brightest sources is described in the following.

5.1.2. Spectral analysis

We selected the subsample of stars for which there are at least 200 events in the source extraction region in the three EPIC instruments together (PN+MOS1+MOS2). Excluding the stars classified as eclipsing or contact binaries, the sample consists of 19 stars. For each one, we extracted the source and background spectrum in the energy band 0.3−10.0 keV, and performed a joint spectral analysis with XSPEC 12.8.1 (Arnaud 1996) of the spectra of all EPIC instruments available for that source. We fit the spectra with an absorbed one-temperature APEC model (`phabs*apec`) or an absorbed two-temperature APEC model (`phabs*(apec+apec)`). We set the coronal abundance to the typical value of 0.2 in solar units (see above) to reduce the number of free parameters and avoid degeneracy.

Two stars showed a significant parameter degeneracy in their spectrum, so we removed them from the analysis. For the stars for which the model requires two temperatures, we calculated an average temperature weighted on the flux of the two APEC components. The results of the best fit for each of the 17 stars, all characterized by a null-hypothesis probability >0.3%, are reported in Table 3. We calculated the average kT over the 17 stars ($\langle kT \rangle$ = 0.83 keV).

With the parameters given in Sect. 5.1.1, we obtained from WebPIMMS the expected flux for each source. We then compared these fluxes with the fluxes obtained from the spectral analysis, for each of the 17 sources for which the spectral fit in XSPEC was performed. For each of these stars we calculated the ratio between the XSPEC flux and the flux from WebPIMMS. For PN, MOS1 and MOS2, we found an average ratio of respectively 0.91, 0.89, 1.00 in the soft energy band 0.2−2.0 keV. We corrected the fluxes obtained with WebPIMMS for the faint (<200 counts) sources by multiplying them with this factor. This correction is meant to obtain from WebPIMMS a flux that is, on average, as close as possible to the actual flux obtained from a spectral fit.

In the sample of 17 bright stars, kT ranges from 0.49 to 1.3 keV. This range is typical for active stars, and the actual plasma temperatures of the bulk of the faint stars is likely in the same range. This span of temperatures introduces an error in the flux calculated with the average kT, allowing fluxes which are up to ~2% lower or ~15% higher than the one calculated from the average temperature of the bright stars. If the 17 X-ray-brightest sources are not representative of our whole sample, these errors may be somewhat larger for the faint stars.

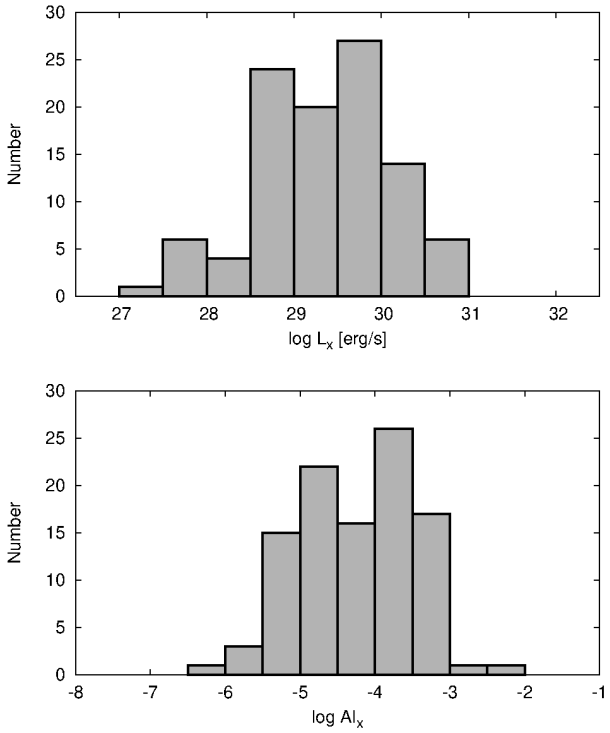

Fig. 6. Distribution of the X-ray luminosity and of the X-ray activity index in the energy band 0.2−2.0 keV for the 102 main-sequence stars.

From the corrected fluxes we calculated the X-ray luminosity using the distances derived in Sect. 3.2. For each source we calculated the X-ray activity index as

$$\mathrm{AI}_X = \frac{L_\mathrm{X}}{L_\mathrm{bol}}. \quad (3)$$

The distributions of the X-ray luminosity and of the corresponding activity index in the soft energy band (0.2−2.0 keV) are reported in Fig. 6. The individual X-ray luminosities are listed in Table A.4.

5.1.3. Considerations on the X-ray luminosity distribution

We compared the distribution of the X-ray luminosity in the range 0.2−2.0 keV for the stars in our sample with those in the NEXXUS sample of Schmitt & Liefke (2004), which consists in a compilation of coronal X-ray emission for nearby late-type stars based on the *ROSAT* observatory. The distribution of the X-ray luminosity for our main-sequence sample and for the one from Schmitt & Liefke (2004) is plotted, for each spectral type and for the whole sample, in Fig. 7.

To first order we consider NEXXUS as a volume-limited sample of nearby stars, representing the full range of X-ray activity of the solar-like stellar population. Note, however, that Stelzer et al. (2013) show that even in as small a volume as 10 pc around the Sun about 40% of the M dwarfs have no X-ray detection in the RASS. From the comparison with our distribution, it is evident that our sample presents a significant bias towards high X-ray luminosities most marked for the latest spectral types reflecting the mass (or T_eff) dependence of X-ray luminosity. The stars in our sample, which is flux-limited, are on average at a much greater distance (see Fig. 7, median distance for the whole sample: ~500 pc). Therefore, we interpret the bias of our sample towards active stars as due to both the X-ray selection and the large distances.

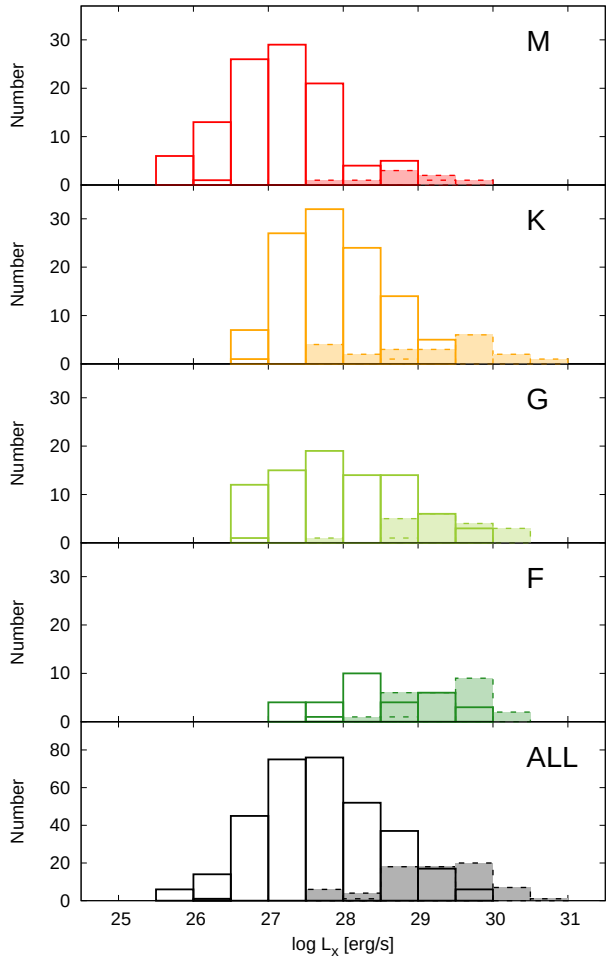

Fig. 7. Distribution of the X-ray luminosity in the energy band 0.2 – 2.0 keV, for the 102 main-sequence stars of the *Kepler* - *XMM-Newton* sample (hatched histograms) and for the NEXXUS stars from Schmitt & Liefke (2004) (solid line) for each spectral type class separately and for all spectral types combined.

5.1.4. X-ray light curves

In order to study the variability of the X-ray emission and to search for X-ray flares, we analyzed the light curves provided by the EXTraS (Exploring the X-ray Transient and variable Sky) project[6] (De Luca et al. 2016). EXTraS was synchronized with 3XMM-DR4, while we are studying X-ray sources from 3XMM-DR5 in the *Kepler* field. Therefore, light curves for observations 0671230201 and 0671230601 are not present in the public EXTraS database, but were produced for this work by the EXTraS team, using the EXTraS analysis pipeline.

EXTraS provides a set of uniform bin light curves with different bin size, from 10 s up to 5000 s and an optimum bin size (chosen to have at least 25 counts in each bin), both for the source and the background extraction regions. In addition, EXTraS also provides light curves produced via an adaptive binning, namely Bayesian blocks (Scargle et al. 2013) algorithm for each source and for the related background region. This algorithm starts with

[6] The EXTraS project (`www.extras-fp7.eu`), aimed at the thorough characterization of the variability of X-ray sources in archival *XMM-Newton* data, was funded within the EU seventh Framework Programme for a data span of 3 yr starting in January 2014. The EXTraS consortium is lead by INAF (Italy) and includes other five institutes in Italy, Germany and the UK.

an initial set of cells defined on the basis of the number of events in the source and background region, and provides a final set of different-duration bins, each of which has a count rate that is not consistent, within 3σ, with the count rate of the adjacent bins.

In the EXTraS analysis pipeline, all the source light curves, both the ones obtained with the uniform bin algorithm and the Bayesian blocks algorithm, are automatically fitted with a series of different models that account for simple variability patterns (constant, linear, quadratic, negative exponential, constant plus flare, constant plus eclipse). This is a standard algorithm that is part of the EXTraS pipeline, and it is applied to all the light curves in the same way. Its purpose is to provide a first-step indication of the kinds of variability possibly present in the light curve, and not to perform a detailed modeling of the variability features observed, nor to determine their parameters. All results are in the database, and online searches can be performed with the query form.

5.1.5. X-ray flaring

For each X-ray source in our sample, we searched for X-ray flares in the EXTraS light curves. First, we inspected the results of the fit performed on the light curves with different variability models by the EXTraS pipeline. As stated above, these results can be used for a first assessment for the kind of variability present in the light curve. If at least one among the uniform bin or adaptive bin light curves is better fitted by a constant plus flare model (higher null-hypothesis probability) than the other models, this is a good indication of a possible flare. This flare model consists of a constant flux level over which a simple flare profile is superimposed, that is a steep linear flux increase, followed by an exponential decay.

The Bayesian blocks light curves are particularly useful to detect flares, which appear as one or more blocks that show a higher flux than the preceeding and following blocks. If the flare occurred at the beginning or at the end of the observation, the Bayesian blocks light curve may show only the rise phase or the decay phase. In this case, we rely on the uniform bin light curves to establish if the event is a true flare or not. We also require that the flare was observed in at least two of the EPIC instruments. The visual inspection of the light curves is however crucial in order to recognize genuine flares, so we inspect all the available EXTraS light curves for each star in our sample.

With this procedure, based on the EXTraS pipeline products we detected 6 X-ray flares on 5 stars, and by visual inspection we identified an additional likely flare on a sixth star, KIC 7018131 (Figs. 8, and 9). In view of the low count statistics of the X-ray lightcurves some remarks on the individual events are in order. KIC 9048976 shows two possible flares: the Bayesian blocks algorithm shows one block with a higher flux at the beginning and at the end of the light curve, impeding the observation of the full flare profile. KIC 8909598 also shows an X-ray flare at the end of the observation. The uniform bin light curves reveal a quite obvious flare profile both in PN and MOS2 cameras. However, this star does not have a reliable main-sequence classification (unknown $\log g$), so we do not consider it in the analysis. For KIC 9048551 the Bayesian block algorithm identifies one flare event, but the uniform bin lightcurve shows evidence of substructure contemporaneous with two events seen in the *Kepler* band.

The X-ray flares shown in Fig. 8 have simultanous white-light flares in the *Kepler* light curves (see Sect. 6.3). Figure 9 displays the light curves for the X-ray flares without a

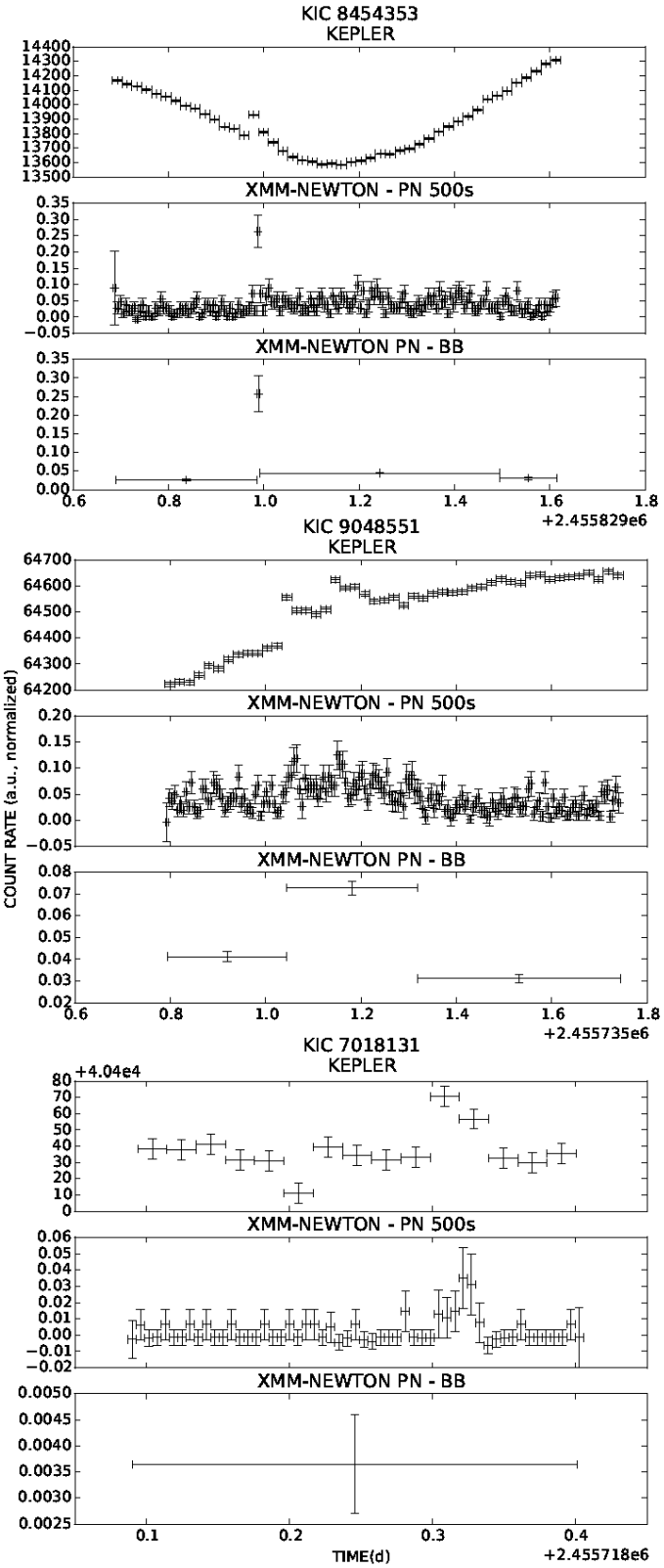

Fig. 8. Simultaneous *Kepler* and *XMM-Newton* EPIC PN light curves for the stars showing a simultaneous X-ray and white-light flare. The EPIC light curves produced by the EXTraS pipeline with 500 s uniform binning and with the Bayesian blocks adaptive binning are plotted. The flare in the *Kepler* light curve of KIC 7018131 corresponds to a bump in the EPIC uniform bin lightcurve which is, however, not significant at a 3σ level over the baseline, and not detected with the Bayesian block algorithm.

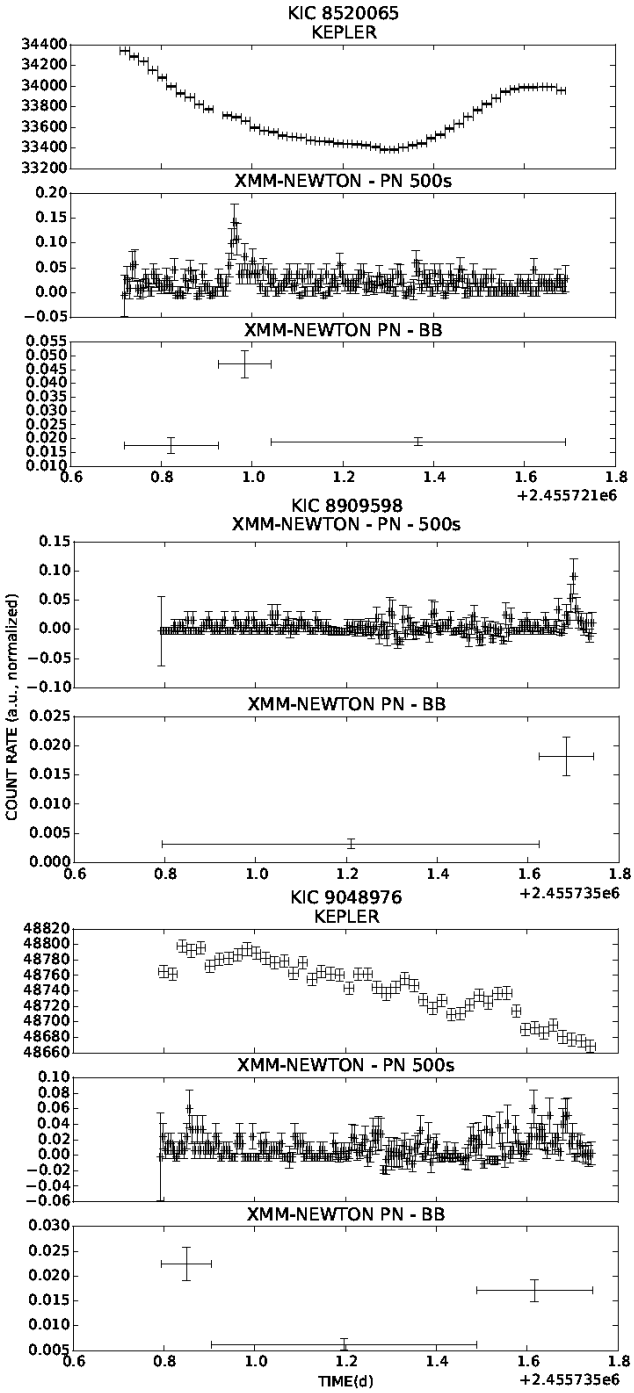

Fig. 9. *XMM-Newton* EPIC PN light curves for the X-ray flares without a white-light counterpart detected by our flare-detection algorithm. Simultaneous *Kepler* light curves are not available for KIC 8909598.

simultaneous white-light counterpart revealed with the flare detection algorithm described in Sect. 4.1. Evidence for a weak increase of the optical brightness at times of the X-ray flare is, however, seen in all the contemporaneous *Kepler* lightcurves.

In Table 4 we report the start time of the X-ray flares (Col. 2), according to the Bayesian blocks light curve except for KIC 7018131, for which we infer the start time from the 500 s uniform bin light curve of EPIC/pn, since the Bayesian blocks light curve has only one block. We also report the quiescent (Col. 3) and peak (Col. 4) X-ray count rate, taken from the 500 s uniform bin light curve of EPIC/pn, together with the overall number of white-light flares observed in the whole *Kepler* light curve for the star (Col. 5), its white-light flare frequency (Col. 6), the average, maximum and minimum peak amplitude of the *Kepler* flares ($A_{\rm peak}$, photometric ratio between the peak bin and the baseline of the flare, Cols. 7 and 8). This parameter is discussed in more detail in Sect. 6.3.1.

5.2. UV activity

The KIC provides UV magnitudes obtained with the Galaxy Evolution Explorer (GALEX). The GALEX satellite performed imaging in two UV bands, far-UV (henceforth FUV; $\lambda_{\rm eff}$ = 1516 Å, $\Delta\lambda$ = 268 Å, and near-UV (henceforth NUV; $\lambda_{\rm eff}$ = 2267 Å, $\Delta\lambda$ = 732 Å). The KIC gives a NUV detection for 71 stars from our main-sequence sample (i.e., 70%) and a FUV detection for 20 main-sequence stars (20%). All but one of the stars with a FUV detection also have a NUV detection. The individual values for the observed NUV and FUV luminosities are listed in Cols. 3 and 4 of Table A.4.

The SED fit provides UV fluxes for the stellar photosphere. In order to validate these measurements, we converted the NUV de-absorbed photospheric fluxes obtained from VOSA into absolute magnitudes and compared the relation between these magnitudes and the $B-V$ color (derived from Pecaut & Mamajek 2013) with the analogous relation observed for a set of photospheric NUV magnitudes provided by Findeisen et al. (2011) in their Table 1. Figure 10 shows that our values are in good agreement with the ones of Findeisen et al. (2011).

For some stars in our sample the observed GALEX NUV and FUV fluxes are significantly higher than the prediction of the best-fitting photosphere model. This UV excess, that is the positive difference between the observed UV flux ($f_{\rm UV,obs}$) and the photospheric flux of the BT-Settl model in the same UV band ($f_{\rm UV,ph}$) represents the UV emission associated with magnetic activity processes in the stellar chromosphere. Following Stelzer et al. (2013), we calculated the corresponding UV activity index as

$$AI'_{\rm UV} = \frac{f_{\rm UV,exc}}{f_{\rm bol}} = \frac{f_{\rm UV,obs} - f_{\rm UV,ph}}{f_{\rm bol}} \quad (4)$$

where $f_{\rm UV,exc}$ is the UV excess flux attributed to activity, and $f_{\rm bol}$ is the bolometric flux. The bolometric flux is obtained from interpolation on the DSEP isochrones, as described in Sect. 3.

We calculated the UV excess in both the GALEX FUV and NUV band, where available. After trying different values and visually inspecting the SED, we found that a threshold of 13% on the ratio between the excess flux and the photospheric expected flux was the best choice to select the stars with a true UV excess. We found 45 main-sequence stars with a NUV excess, ten of them display also a FUV excess, and an additional 4 have a FUV excess but no NUV excess. The NUV and FUV excess luminosities are provided in Cols. 5 and 6 of Table A.4.

6. Results and discussion

6.1. Rotation periods

For 74 main-sequence stars out of 102 (73%) the *Kepler* light curve is dominated by the rotational brightness modulation due to starspots, with a period in the explored range $P_{\rm rot} < 90$ d. For the individual spectral types, the fraction of main-sequence stars with a rotational brightness modulation is: A 66% (2/3), F 65% (24/37), G 73% (19/26), K 75% (21/28) and M 100% (8/8). Our

Table 4. Parameters of the X-ray flares and *Kepler* flare characteristic of the X-ray flaring stars.

KIC_ID	Start time (Julian day)	$\mathrm{Rate_{X,quiesc}}$ (cts $\mathrm{s^{-1}}$)	$\mathrm{Rate_{X,peak}}$ (cts $\mathrm{s^{-1}}$)	$N_{\mathrm{opt,flares}}$	$F_{\mathrm{opt,flares}}$ ($\mathrm{d^{-1}}$)	$\langle \log A_{\mathrm{peak}} \rangle$	Min-max $\log A_{\mathrm{peak}}$
7 018 131	2455718.31	0.006 ± 0.011	0.035 ± 0.019	5	0.005	−2.79	−2.89/−2.67
8 454 353	2455829.96	0.036 ± 0.020	0.263 ± 0.048	297	0.211	−1.86	−0.36/−2.69
8 520 065	2455721.96	0.020 ± 0.016	0.140 ± 0.040	0	0	0	0
8 909 598	2455736.55	0.004 ± 0.011	0.090 ± 0.003	7	0.022	−1.83	−1.43/−2.21
9 048 551	2455736.03	0.033 ± 0.016	0.125 ± 0.028	233	0.164	−2.41	−1.47/−2.92
9 048 976	2455735.94,2455736.80	0.009 ± 0.013	0.06 ± 0.02,0.060 ± 0.024	137	0.097	−2.37	−1.57/−2.91

Notes. The start time of each X-ray flare is reported, together with the peak and off-flare count rate. The number and the frequency of the white-light flares observed for the star is also given, together with the average, minimum and maximum peak amplitude of all its white-light flares in the *Kepler* light curve.

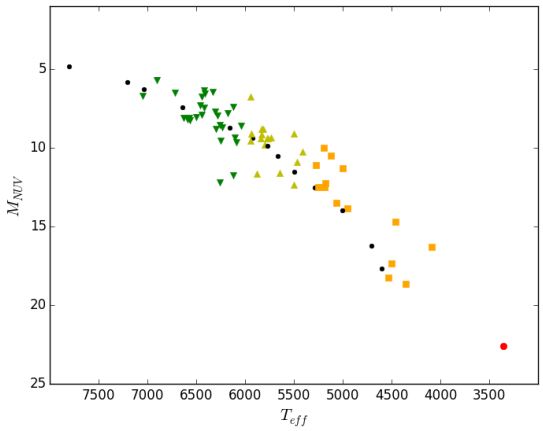

Fig. 10. Absolute NUV magnitude versus Johnson color *B–V* for the stars in our sample with a GALEX NUV detection, for each spectral type, and for the values of Table 1 in Findeisen et al. (2011) (black dots). Different symbols represent the spectral type; red circles: M, orange squares: K, light-green triangle up: G, dark-green triangle down: F.

period detection rate is higher with respect to other studies based on *Kepler* data (McQuillan et al. 2013, 2014, 37% in the range $3500\,\mathrm{K} < T_{\mathrm{eff}} < 6500\,\mathrm{K}$, F ∼27%, G ∼25%, K ∼60%, M ∼80%; Stelzer et al. 2016, 73% for M dwarfs). This is probably an effect of the selection bias towards active (and thus strongly spotted) stars as well as the removal of giant stars from our sample.

In Table 2 a summary of the number of stars with rotation period from our analysis is reported for every spectral type, together with the number of stars with other types of brightness modulation patterns. We refer to Table A.2 for the classification of the photometric variability for each star in the sample.

Only 54 stars out of 74 have previously reported periods from McQuillan et al. (2014), obtained from the same *Kepler* light curves. For the 54 stars for which a rotation period is reported in McQuillan et al. (2014), those periods are consistent with our values within uncertainties. The remaining 20 stars do not have any previously determined period in the literature.

6.2. Activity-rotation relation

In Fig. 11, we present the relation between the X-ray luminosity in the soft energy band 0.2–2.0 keV and the rotation period, together with the relation between the X-ray activity index (defined in Eq. (3)) and the Rossby number. A clear decrease in X-ray activity levels is observed for slower rotators. This effect is more evident in the $\mathrm{AI_x}$ versus Rossby number plot, and produces a "kink" in the distribution, which can be seen quite clearly in the overall sample of all stars, and also in the subsamples of K stars, while for M, G and F stars it is not obvious as these subsamples comprise only a limited range of rotation rates. The "kink" suggests the presence of a correlated regime for slow rotators, and of a saturated regime for fast rotators, with a separation occurring at ∼8 d (from visual inspection). The wide range of L_X and $\mathrm{AI_X}$ independent of P_{rot} for the (generally fast rotating) F stars is remarkable: it is possible that the F stars present a decoupling between rotation and activity because of their shallow convective zones. This group may also include active binary stars (RS CVn) with unknown contribution to the X-ray emission from the cool companions.

In Fig. 11 we show for comparison the literature compilation from Wright et al. (2011) and the previous empirical relations obtained by Pizzolato et al. (2003) based on a small sample with mostly spectroscopic rotation measurements (solid lines). The rotation periods in Wright et al. (2011) were collected from several works which use both spectroscopic and photometric techniques, and the X-ray fluxes were obtained from the analysis of data taken from different missions, such as *XMM-Newton* and *ROSAT*. We find excellent agreement of our more homogeneous data with that study. Especially, the scatter clearly decreases when X-ray luminosity and rotation period are replaced by $\mathrm{AI_x}$ and R_0, respectively. Contrary to previous work where no uncertainties were estimated, we present here conservative error bars for our sample. These are dominated by the uncertainties in the distances of stars without *Gaia* parallax that are derived from mapping the stars in the $\log g - \log T_{\mathrm{eff}}$ diagram onto the Dartmouth isochrones (see Sect. 3.2), meaning that they ultimately go back to the uncertainties in the spectroscopic parameters.

The rotation-activity relation of M dwarfs in our sample can be compared to that of M dwarfs observed in the K2 mission studied by Stelzer et al. (2016) with an analogous approach. In Fig. 12 we show the $L_{\mathrm{x}} - P_{\mathrm{rot}}$ relation for the two samples. Our X-ray selection evidently excludes slowly rotating M stars in the non-saturated regime. This can also be seen from the comparison with the bimodal relation suggested by Pizzolato et al. (2003) (solid black line in Fig. 11) which is, however, itself extremely poorly defined. Recent M dwarf studies by Wright & Drake (2016) and Wright et al. (2018), also shown in the figure, used rotation periods measured with ground-based instruments. They cover the long-period "correlated" region and are complementary to our *Kepler* study.

The scatter observed in the saturated regime of L_{X} and AI_{x} for M stars of given P_{rot} is large but consistent with that observed by Wright et al. (2011), Pizzolato et al. (2003) and Stelzer et al. (2016), and probably due, at least in part, to the spectral type distribution within the M class, with cooler stars having lower

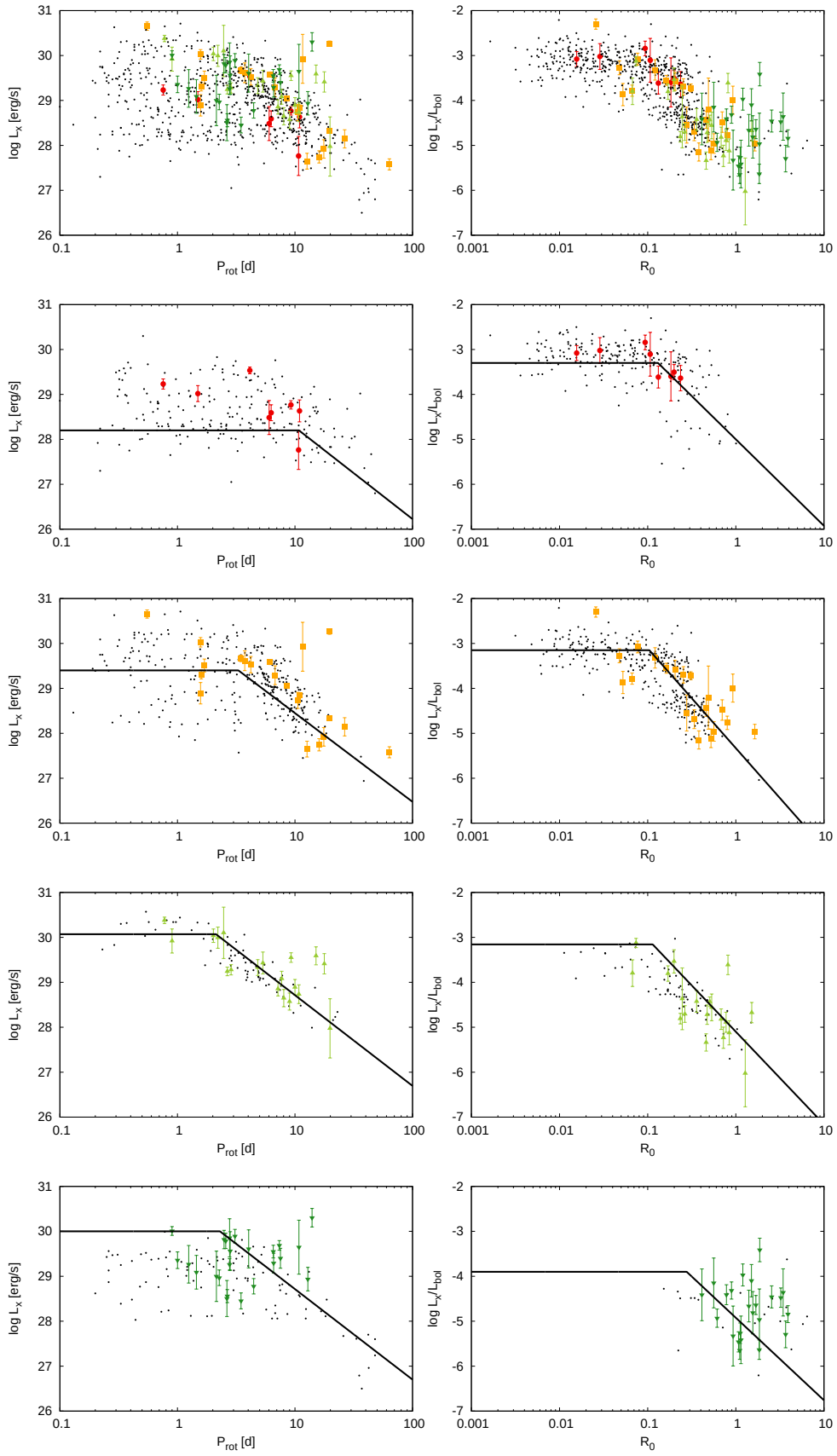

Fig. 11. X-ray activity versus rotation for the full sample, M-, K-, G-, and F-type stars (*from top to bottom*). *Left panels*: X-ray luminosity in the energy band 0.2−2.0 keV versus *Kepler* P_{rot}. *Right panels*: X-ray activity index versus Rossby number. Colours and symbols follow the convention defined in Fig. 10. The stars in the sample of Wright et al. (2011) are shown as small black dots. The solid lines represent the best-fit relations between X-ray emission and rotation period found by Pizzolato et al. (2003) for stellar mass ranges corresponding approximately to spectral types.

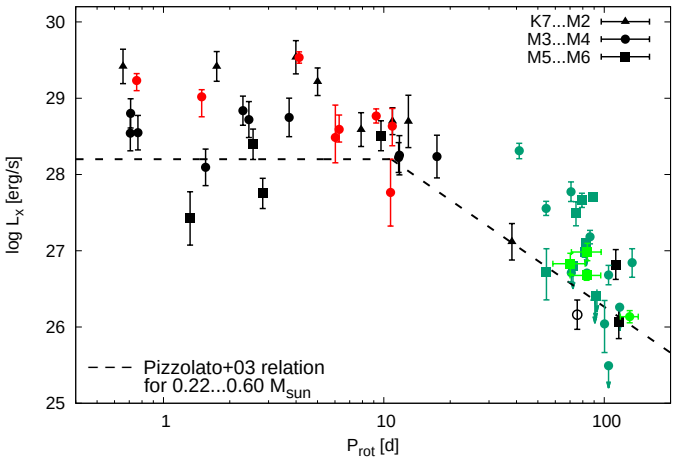

Fig. 12. L_X vs. P_{rot} for M dwarfs: red – this work, black – K2 sample from Stelzer et al. (2016) (their Fig. 15), green – stars published by Wright & Drake (2016) and Wright et al. (2018). The solid line represents the best-fit rotation-activity relation from Pizzolato et al. (2003) in the range 0.22–0.60 $M_\odot$.

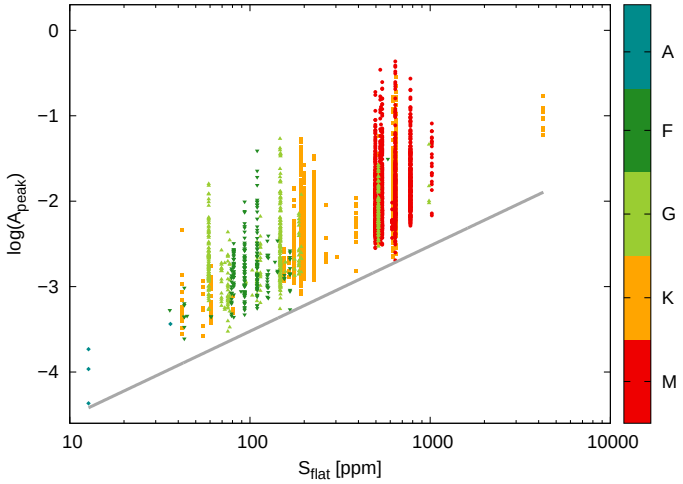

Fig. 13. Relative peak amplitudes of all detected optical flares in the *Kepler* lightcurves measured with respect to the flattened lightcurve. The gray line denotes our threshold for flare detection set to $3 \times S_{flat}$.

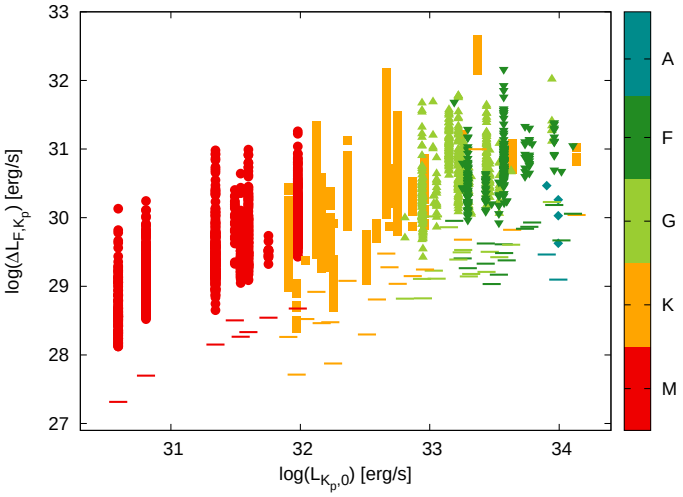

Fig. 14. Absolute flare amplitudes versus quiescent luminosity represented by the *Kepler* magnitude associated with the flattened lightcurve; see text for details.

X-ray luminosity. The scatter decreases when considering the relation AI_x versus R_0. Because of the relatively low statistics in our sample, in particular the low number of stars in the correlated regime, it would be difficult to establish with good confidence the turnover point between the correlated and saturated regime, nor the slope of the correlated part of the relation.

6.3. Kepler activity diagnostics

6.3.1. Optical flares

We explore here the optical flaring activity measured in the *Kepler* lightcurves of the spotted stars. This analysis must consider that the sensitivity for detecting flares depends on the (quiescent) brightness of the star and is different for each star. The criteria in our definition of flare include a $\geq 3\sigma$ upward deviation from the flattened lightcurve (see Sect. 4.1). As a result of the relation between K_p and spectral type in our sample (evident in Fig. 5), the minimum measurable flare amplitude (A_{peak}) – defined here as the relative brightness difference between the flare peak and the flattened lightcurve – shows a trend with spectral type (Fig. 13).

For a meaningful comparison of our sample which covers a large range in brightness we must convert relative quantities, such as A_{peak} and S_{flat}, to absolute ones. The *Kepler* photometry is not flux calibrated. However, an approximate brightness can be associated to the flattened lightcurve assuming that this normalized "quiescent" emission corresponds to the *Kepler* magnitude of the star. We convert K_p to flux using the zero-point and effective bandwidth provided at the filter profile service of the Spanish Virtual Observatory (SVO)[7]. Then we apply the distances derived in Sect. 3.2 to obtain the "quiescent" luminosity in the *Kepler* band, $L_{K_p,0}$. Similarly, the flare amplitude is converted from its relative value (A_{peak}) to a luminosity, $\Delta L_{F,K_p} = L_{K_p,0} \times A_{peak}$. The resulting relation between flare amplitude (in erg s^{-1}) and quiescent luminosity is shown in Fig. 14. The lower envelope is defined by our flare detection threshold which is marked as a horizontal bar for each star and which is rising with increasing stellar luminosity. The A-type stars form an exception to this trend. They show lower flare amplitudes than expected for their $L_{K_p,0}$. This finding can easily be explained when the observed flares are attributed to unknown and unresolved later-type companion stars. In this scenario the actual $L_{K_p,0}$ value of the flare-host would be lower making the true amplitude $\Delta L_{F,K_p}$ higher than measured. This would shift the data points to the left and upwards in Fig. 14.

For a given star, the range of flare luminosities, $\Delta L_{F,K_p}$, extends up to ~2 orders of magnitude above the amplitude of the minimum observable flare. The range of flare amplitudes is smaller for G and F stars but this is probably related to the lack of sensitivity for the detection of low-luminosity flares. This is evident from consideration of the S_{flat} values which set the detection threshold (see Figs. 13 and 14).

One of the aims of our study is the investigation of a connection between flaring activity and rotation rate. In their analogous study on M dwarfs observed in the K2 mission, Stelzer et al. (2016) have found a sharp transition in the optical flaring behavior at a period of ~10 d. This transition is difficult to probe with this X-ray selected *Kepler* sample for two reasons: (1) the small number of slow rotators and (2) the broad range of K_p translating

[7] http://svo2.cab.inta-csic.es/svo/theory/fps/

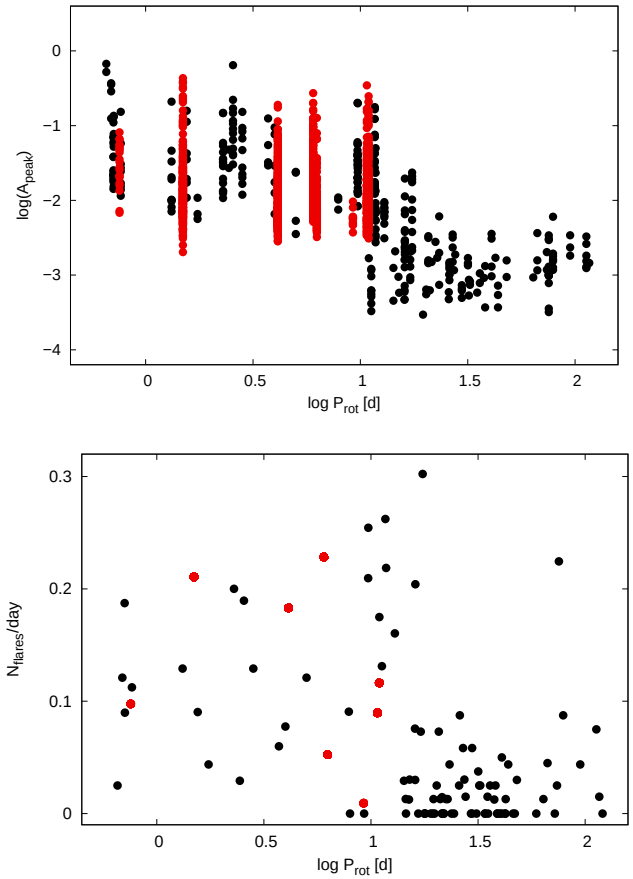

Fig. 15. Relative flare amplitudes ($A_{\rm peak}$; *top panel*) and flare frequency (*bottom panel*) versus rotation period for the M stars in our *Kepler* sample (red) and for the M stars of the K2 sample presented by Stelzer et al. (2016) (black).

into a dishomogeneous flare detection threshold. If we restrict our sample to M dwarfs which span a relatively narrow range in optical brightness (cf. Fig. 5), the relative flare amplitudes and the flare frequencies are consistent with the results obtained by Stelzer et al. (2016) but we are covering only the fast periods up to the presumed transition (see Fig. 15). The average flare frequency of the M stars in our sample (0.12 flares d^{-1}) is in excellent agreement with the average flare frequency in Stelzer et al. (2016) calculated over the $P_{\rm rot}$ range ($P_{\rm rot} \lesssim 10$ d) covered by the *Kepler* M stars (0.11 flares d^{-1}). This shows that our *Kepler* sample, albeit highly incomplete at the slow-rotation and low-activity side, is representative for fast rotating and active M dwarfs.

Analogous to the study of Stelzer et al. (2016) on K2 lightcurves, the sampling time of 29.4 min of the *Kepler* lightcurves used in this work, together with the characteristics of the flare search algorithm (see Sect. 4.3), prevent the detection of flares with duration below ∼1 h. As a consequence, we detect mostly flares with large-amplitude and relatively long duration. It can be suspected that there is a significant population of smaller and shorter flares that cannot be observed, due to the long cadence of the light curves and to the flare-extraction pipeline. Therefore, the flare frequencies of Fig. 15 and Table 5 likely represent a lower limit to the actual values.

6.3.2. X-ray versus white-light flares

As described in Sect. 5.1.5 we find seven X-ray flares on six stars. For these events the count rate at the flare peak (as measured from the EXTraS Bayesian light curves) is a factor 3−7 higher than during the non-flaring, quiescent time-intervals. As a result of the large distances of the *Kepler* stars, the X-ray count rates are small and the low counts statistics prevent a detailed quantitative analysis such as the determination of decay time and total flare energy.

All the stars with an X-ray flare except KIC 8909598 are classified as main-sequence: one M-type, three K-type and one F-type star. We do not consider KIC 8909598 in the further analysis. All but the F star (KIC 8520065), show a clear rotational modulation in their *Kepler* light curves. This latter one is according to our analysis probably also a rotator, but the variability pattern is unclear, and it is not possible to estimate a reliable rotation period.

We compare the X-ray flaring with the white-light flaring activity. Of the four stars with a detected rotation period, three show a large number of white-light flares in the *Kepler* lightcurves, and are among the stars with the highest optical flare frequency. This underlines the strong connection between X-ray and optical flaring mechanism: since the X-ray observations are relatively short in duration, X-ray flares are observed predominantly in the light curves of the stars which show a higher optical flare frequency. There are simultaneous *XMM-Newton*/*Kepler* observations for 69 stars in our sample. All the X-ray flaring stars in our sample (except for KIC 8909598, which, as mentioned, we exclude from the analysis) have a *Kepler* observation simultaneous with the *XMM-Newton* observation in which the X-ray flare was detected. No white-light flares without X-ray counterpart were detected during the simultaneous X-ray and white-light observations.

Our automated *Kepler* flare-detection algorithm finds 3 events occurring within ∼1 h from the observed X-ray flares (see Fig. 8). However, visual inspection shows that the other X-ray flares likely have optical counterparts as well, which have remained below the detection threshold of our automatic algorithm. Finally, a simultaneous event, detected only by visual inspection of the X-ray (and *Kepler*) lightcurves, occurred on one star. To summarize, of the 6 X-ray flares observed from rotating dwarf stars, there is evidence for a contemporaneous optical event in all cases, but only for three of them is the associated white-light flare clearly detected (one M-type and two K-type stars).

Table 5. Mean values and standard deviations measured for photometric activity diagnostics in the *Kepler*/*XMM-Newton* sample.

SpT	$N_{\rm f}$/day	$\log R_{\rm per}$ (%)	$S_{\rm ph}$(ppm)
A	0.001	−1.02	3.47×10^2
F	0.01	−0.74	1.10×10^3
G	0.02	0.01	5.39×10^3
K	0.04	0.25	8.69×10^3
M	0.12	0.46	1.10×10^4

6.3.3. Other Kepler activity diagnostics

Here we examine the distribution of the photospheric activity diagnostics $S_{\rm ph}$ and $R_{\rm per}$ (see Sect. 4.4 for their definition). As mentioned above, as a result of the bias to active stars, our *Kepler* sample does not allow us to study the transition of the optical activity diagnostics at $P_{\rm rot} \sim 10$ d revealed in the K2 data of nearby M dwarfs. Figure 16 shows our M dwarf sample compared to the one studied by Stelzer et al. (2016). Similar to the

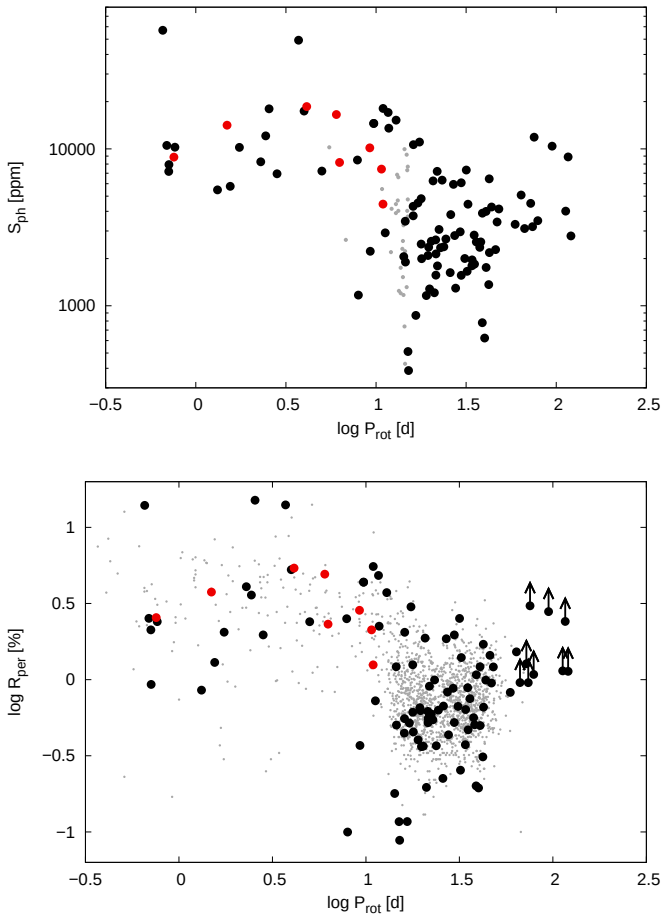

Fig. 16. Photometric activity diagnostics versus rotation period for M stars. Red dots – M stars in our sample; black dots – K2 M dwarf sample of Stelzer et al. (2016); gray dots – field M dwarfs in the sample by Mathur et al. (2014a) in the *top panel* and field M dwarfs from McQuillan et al. (2013) in the *bottom panel*.

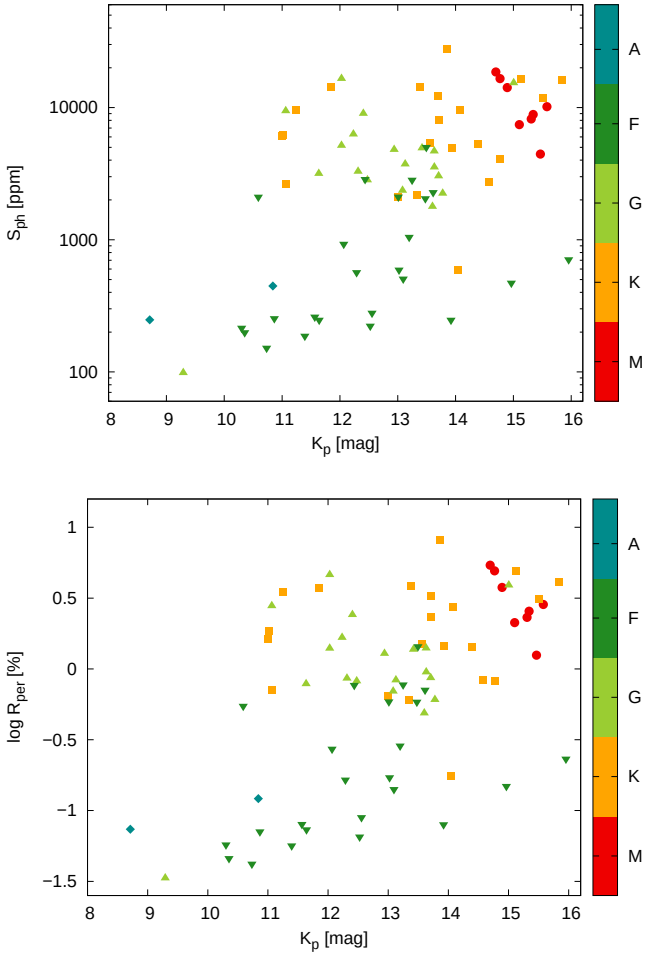

Fig. 17. Photometric activity diagnostics versus *Kepler* magnitude for the stars in our *Kepler*/*XMM-Newton* sample divided in spectral type bins. *Top*: S_{ph} versus *Kepler* magnitude; *Bottom*: $\log R_{per}$ versus *Kepler* magnitude.

results on optical flares, the rotation cycle amplitude (R_{per}) and the overall variability of the lightcurve (S_{ph}) of the two samples follow the same distribution in the fast-rotator regime.

We can examine the spectral type dependence of the photometric activity diagnostics, provided that – analogous to the detection of flares – the brightness dependence of the sensitivity for measuring variations is considered. In Fig. 17 we display S_{ph} and R_{per}, versus K_p separately for each spectral class. The average values of S_{ph} and R_{per} for each spectral type are listed in Table 5. While the exclusively high values for the activity diagnostics in the M dwarfs may be due to their faintness, preventing the detection of small variations, a curious distinction is seen for F stars. Albeit covering roughly the same level of (quiescent) brightness in the *Kepler* band as the G dwarfs and some of the K dwarfs and the same range of P_{rot} (see e.g. Fig. 11), the variability of the F stars is markedly smaller. This points at intrinsically weaker variability in F stars. A similar effect is seen in Fig. 4 of McQuillan et al. (2014). Our finding is aggravated by the fact that the F stars of our sample are more active, that is have higher S_{ph} values, than a sample of 22 F stars selected from the *Kepler* Asteroseismic Science Consortium (KASC) programme studied by Mathur et al. (2014b).

6.4. UV activity

As this sample is X-ray selected, all stars for which we detected an UV excess have an X-ray detection. We show in Fig. 18 the correlation between the UV excess luminosity (as calculated in Sect. 5.2) and the X-ray luminosity. With the caveat that the GALEX filters exclude some important chromospheric contributions, most notably the Mg II doublet, these relations represent a comparison of the chromospheric and the coronal radiative energy output. The sample with FUV excess is too small for any conclusion. We perform the Spearman's and Kendall's correlation tests for the NUV and X-ray luminosities of each SpT and find that only the K stars show a significant positive correlation between the two luminosities (p-values < 0.05) with rank correlation coefficients $\rho_s = 0.85$ and $\rho_K = 0.64$. The F and G stars show each a considerable spread in the distribution, similar to the behavior of the F stars in the X-ray-rotation relation of Fig. 11.

We also compare the UV emission levels of our sample to the UV emission of the exoplanet hosts studied by Shkolnik (2013). Deviating from the remainder of this paper, which is focused on the high-energy emission due to stellar activity, we consider here the total observed UV emission which includes photospheric plus chromospheric contribution. This enables a direct comparison to the work of Shkolnik (2013). Secondly, for the irradiation of exoplanets the relevant parameter is the total UV output of the star irrespective of its origin. Figure 19 shows the distribution of L_{NUV}/L_{bol} versus T_{eff} for our stars and for the sample of exoplanet hosts analyzed by Shkolnik (2013). Our UV luminosity values are for given T_{eff} about one order of magnitude above the values of the stars with exoplanets. This might be explained by

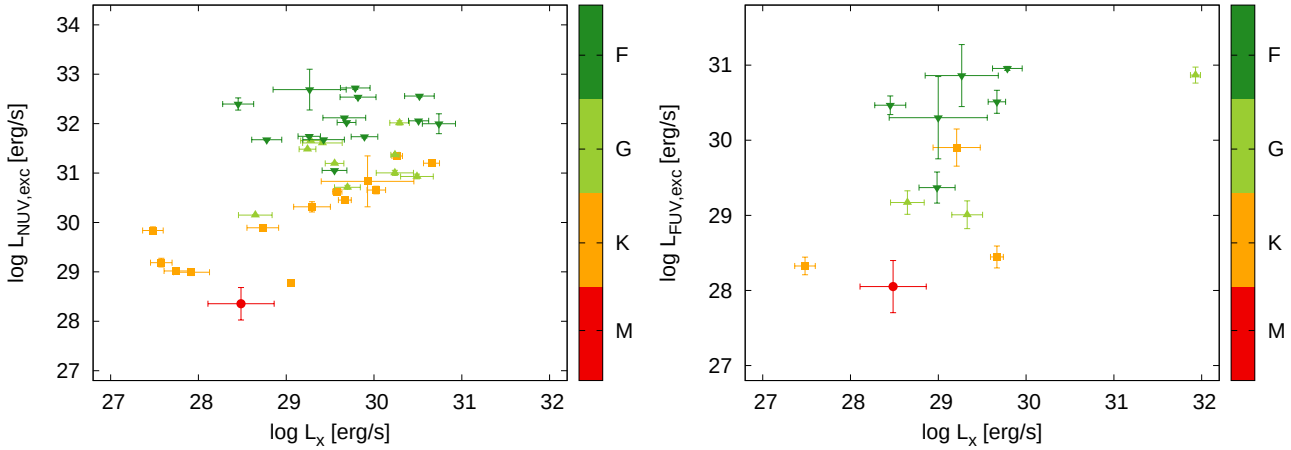

Fig. 18. UV chromospheric excess luminosity versus X-ray luminosity for the full sample.

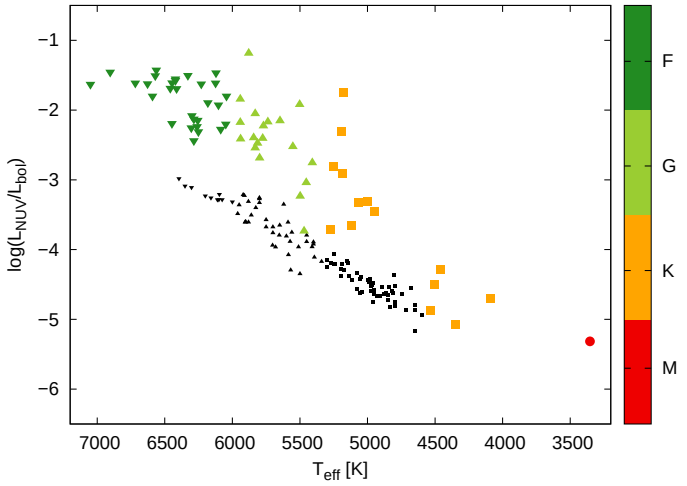

Fig. 19. Observed fractional NUV luminosity versus $T_{\rm eff}$ for the stars in our sample (with the usual color code) and the ones from Shkolnik (2013, black dots).

an oppositely directed bias in both samples: While our sample is biased towards active stars, known exoplanet hosts are typically inactive as a result of the selection criteria for planet search programs. A second reason that might influence the differences between the NUV emission of the two samples is the fact that the stars in the sample of Shkolnik (2013) are typically nearby (tens of parsec), such that many stars were saturated in the GALEX observations and they have been removed from the analysis, thus generating a bias towards small NUV luminosity. Based on these arguments, there is good reason to believe that the two samples taken together represent the full range of NUV luminosity for each spectral type.

6.5. A-type stars

Three stars in our sample are classified as A-type on the basis of their effective temperature. The light curve of one of them (KIC 5113797) shows a variability pattern that suggests an association with the class of γ Dor non-radial pulsators. The others (KIC 8703413, KIC 9048114) have a clear rotational modulation pattern suggesting the presence of star spots. Only 3 flares have been detected by our algorithm in the *Kepler* lightcurves of the A stars in our sample.

Late A-type stars represent the high-mass borderline of the magnetically active stars. A change in the stellar structure occurs with respect to later-type stars: the outer convective layer disappears, leaving a fully radiative stellar interior. It is generally believed that the standard stellar dynamo model can not be applied to fully radiative stars, which lack the transition between convective and radiative zones. Dynamos may operate in the small convective cores of hot stars, but a major problem is the emergence of the ensuing fields to the surface of the stars where magnetic activity is observed. Considering these difficulties, the magnetic activity apparently observed on A-type stars, and especially the X-ray emission, is often ascribed to unresolved late-type companion stars in binary systems. In a systematic study of a large sample of A-type stars associated with a *ROSAT* X-ray source about 25% are bona-fide single stars (Schröder & Schmitt 2007), and the question on whether A-type stars can maintain a corona has not been conclusively resolved.

Similarly, the occurrence of photospheric magnetic activity in A-type stars is disputed. Balona (2013, 2015) performed a search for activity in the A stars observed by *Kepler*. Both rotational variability due to starspots and flaring activity was detected for a significant fraction of stars. Two A stars from our sample (KIC 8703413 and KIC 5113797) were classified as flaring stars by Balona (2013, 2015). The authors considered the flares on *Kepler* A-type too energetic to be attributed to possible late-type companions. However, this result has been refuted by Pedersen et al. (2016).

The $T_{\rm eff}$ of the three stars classified as A-type present in the *Kepler*/*XMM-Newton* sample is below the limit set by Simon et al. (2002) for the fully radiative regime (8250 *K*) within uncertainties. KIC 9048114 is also consistent, within uncertainties, with an early-F type classification. The detection of activity from these stars may thus not be inconsistent with the standard dynamo model.

7. Conclusions

Using a complex sample selection approach involving multi-band photometric characterization and visual inspection of multi-band images, we identify 125 stars with X-ray detection in the 3XMM-DR5 catalog that are observed by the *Kepler* mission. The subsample of 102 dwarf stars studied in this work comprises stars with spectral types from A to M. The distance of these stars range between ~40−7400 pc, with 90% of the stars in the range ~40−1500 pc. By comparison to the volume-limited

NEXXUS sample of nearby stars (Schmitt & Liefke 2004) we estimate that – as a result of the X-ray selection and the large distances of the *Kepler* stars – we probe only the most active 10% of the stellar main-sequence population.

A previous survey of the X-ray (and UV) activity of *Kepler* objects was performed by Smith et al. (2015), in which ~1/5 of the *Kepler* field of view was surveyed with the *Swift* instruments XRT and UVOT (X-ray sensitivity in the energy range 0.2−10 keV : 2×10^{-14} erg cm^{-2} s^{-1} in 10^4 s). Ninety-three KIC objects were found to have an X-ray counterpart, of which 33 were recognized as stars. None of the 20 X-ray emitting stars from our joint *Kepler*/*XMM-Newton* study that are in the *Swift* FoV was detected by *Swift*. This is not surprising, as the average sensitivity limit of the *XMM-Newton* observations in the *Kepler* field is about a factor 3 deeper than the *Swift* observations (see Table 1 for the range of flux limits for our data set).

In the *Kepler* light curves of the XMM-DR5 selected sample, we found several types of variability: rotational modulation due to spots, eclipsing binary systems, multi-periodicity possibly associated with rotational modulation in binary systems, contact binaries, variability due to stellar pulsations (δ Sct and γ Dor stars), uncorrelated and confuse variability patterns. A large fraction of the stars present rotational modulation due to starspots (74, ~73% of the dwarf stars in the sample). The number of stars with rotational modulation may represent a lower limit, since other stars may have a weak rotational modulation which cannot be ascertained with sufficient confidence, or the rotational modulation is superimposed on other kinds of variability, as e.g., in the above-mentioned probable binary systems. The maximum period detectable is limited by the length of the *Kepler* Quarters (~90 d). We found periods in the range 0.3−70 d, with a distribution which does not present significant differences from one spectral type to the other.

We explored the relation of several photometric activity indicators and the coronal X-ray emission with the rotation period. Our data confirm previously observed values and ranges for the rotation-dependence of the star-spot brightness amplitude ($R_{\rm per}$), the overall variability (characterized by the standard deviation of the lightcurve $S_{\rm ph}$) and the residual noise after subtraction of rotational modulation and flares ($S_{\rm flat}$). Due to the predominance of fast rotators in our sample, the bimodality observed in previous works on M dwarfs (Stelzer et al. 2016), with a sharp transition between fast and slow rotators, can not be studied at the same detail. We do find, however, no evidence for high flare rates and amplitudes in the slow rotator regime above $P_{\rm rot} \sim 10$ d, in line with the expectation from these previous findings.

The $R_{\rm per}$ and $S_{\rm ph}$ values of the F stars appear underluminous with respect to later-type stars at the same intrinsic brightness, indicating that this result is not a bias. The same effect was seen in larger and less biased samples, e.g. by McQuillan et al. (2014). Unresolved late-type companion stars are a possible explanation for the low amplitude of the rotational modulation of the F stars. The rotational signal might actually be from such an unknown late-type star, diluted by the bright F star that dominates the unmodulated flux. Alternatively, the low $R_{\rm per}$ and $S_{\rm ph}$ values of the F stars may mark decreasing spot filling factor towards the high-mass limit of partially convective, dynamo-driving stars.

To examine the relation between X-ray activity and rotation we have composed L_X vs. $P_{\rm rot}$ and $L_X/L_{\rm bol}$ vs. Rossby number (R_0) plot. A kink in the rotation-X-ray relation is observed, traditionally described as a transition between a saturated and a correlated regime. The resulting distributions confirm earlier studies of this parameter space using here a much more homogeneous dataset (X-ray data and rotation periods from a single instrument, each) and analysis (same flare and rotation search mechanism for all stars). Similar to the most extensive sample studied previously in this respect, Wright et al. (2011), the saturated and correlated regime are hard to define for subsamples divided by spectral type. The reason is that in the representation involving Rossby number (where the two regimes are usually more marked than when using $P_{\rm rot}$) individual spectral types cover either only the saturated part (M stars) or only the correlated part (FGK stars).

We note that the F stars seem not to participate in the downward trend of the X-ray emission in the $P_{\rm rot}$ (or R_0) range representing the "correlated" zone for the later spectral types. Also, contrary to the other spectral types, the F stars show no clear correlation between X-ray luminosity and UV excess luminosity. Within the group of F stars there is no correlation of X-ray or UV excess with $T_{\rm eff}$. It is therefore not obvious to ascribe this finding to the transition to fully radiative interior with the ensuing break-down of the solar-type dynamo. One possibility for the disordinated behavior of the F stars is that this group may comprise close binary stars with a later type companion star confusing the activity pattern. In such unresolved binaries the measured period might actually represent the rotation of the (unknown) later-type star with implications on all relations involving $P_{\rm rot}$. In fact, we observe in Fig. 11 that both the range of periods and the range of observed $L_{\rm x}$ are similar for M stars and F stars. This scenario would explain the absence of a correlation between $P_{\rm rot}$ and $L_{\rm x}$ as the longest observed periods (~10 d) are still within the range of the "canonical" saturated regime for M dwarfs.

A major asset of this study is the fact that 9 of the *XMM-Newton* observations were carried out during the *Kepler* monitoring, providing strictly simultaneous optical and X-ray lightcurves. We discovered seven X-ray flares. For all of them there is evidence of a white-light counterpart in the *Kepler* lightcurves.

Acknowledgements. This work is based on observations obtained with the *Kepler* mission and with *XMM-Newton*. Funding for the *Kepler* mission is provided by the NASA Science Mission directorate. *XMM-Newton* is an ESA science mission with instruments and contributions directly funded by ESA Member States and NASA. We have made use of data produced by the EXTraS project, funded by the European Union's Seventh Framework Programme, and we acknowledge its financial support under grant agreement no. 607452 (EXTraS project) and that of the Italian Space Agency (ASI) through the ASI-INAF agreement 2017-14-H.0. This work also includes data from the European Space Agency (ESA) mission *Gaia* (`https://www.cosmos.esa.int/gaia`), processed by the *Gaia* Data Processing and Analysis Consortium (DPAC, `https://www.cosmos.esa.int/web/gaia/dpac/consortium`). Funding for the DPAC has been provided by national institutions, in particular the institutions participating in the *Gaia* Multilateral Agreement. This research has made use of the SVO Filter Profile Service (`http://svo2.cab.inta-csic.es/theory/fps/`) supported from the Spanish MINECO through grant AyA2014-55216 and of VOSA, developed under the Spanish Virtual Observatory project supported from the Spanish MICINN through grants AYA2008-02156 and AYA2011-24052.

References

Allard, F., Homeier, D., & Freytag, B. 2012, Phil. Trans. R. Soc. London, Ser. A, 370, 2765
Arenou, F., Luri, X., Babusiaux, C., et al. 2018, A&A, 616, A17
Arnaud, K. A. 1996, in, Astronomical Data Analysis Software and Systems V, eds. G. H. Jacoby & J. Barnes, ASP Conf. Ser., 101, 17
Balona, L. A. 2013, MNRAS, 431, 2240
Balona, L. A. 2015, MNRAS, 447, 2714
Basri, G., Walkowicz, L. M., & Reiners, A. 2013, ApJ, 769, 37
Bayo, A., Rodrigo, C., Barrado, Y., Navascués, D., et al. 2008, A&A, 492, 277
Boch, T., & Fernique, P. 2014, in Astronomical Data Analysis Software and Systems XXIII, ed. N. Manset & P. Forshay, ASP Conf. Ser., 485, 277

Bonnarel, F., Fernique, P., Bienaymé, O., et al. 2000, A&AS, 143, 33
Brown, T. M., Latham, D. W., Everett, M. E., & Esquerdo, G. A. 2011, AJ, 142, 112
Cardelli, J. A., Clayton, G. C., & Mathis, J. S. 1989, ApJ, 345, 245
Cranmer, S. R., & Saar, S. H. 2011, ApJ, 741, 54
De Luca, A., Salvaterra, R., Tiengo, A., et al. 2016, Astrophys. Space Sci. Proc. (Switzerland: Springer International Publishing), 42, 291
Dobson, A. K., & Radick, R. R. 1989, ApJ, 344, 907
Dotter, A., Chaboyer, B., Jevremović, D., et al. 2008, ApJS, 178, 89
Findeisen, K., Hillenbrand, L., & Soderblom, D. 2011, AJ, 142, 23
Frasca, A., Molenda-Zakowicz, J., De Cat, P., et al. 2016, A&A, 594, A39
Gaia Collaboration (Brown, A. G. A., et al.) 2018, A&A, 616, A1
He, H., Wang, H., & Yun, D. 2015, ApJS, 221, 18
Huber, D., Silva Aguirre, V., Matthews, J. M., et al. 2014, ApJS, 211, 2
Jardine, M., & Unruh, Y. C. 1999, A&A, 346, 883
Kalberla, P. M. W., Burton, W. B., Hartmann, D., et al. 2005, A&A, 440, 775
Kraft, R. P. 1967, ApJ, 150, 551
Lindegren, L., Hernández, J., Bombrun, A., et al. 2018, A&A, 616, A2
Mathur, S., Salabert, D., García, R. A., & Ceillier, T. 2014a, J. Space Weather Space Climate, 4, A15
Mathur, S., García, R. A., Ballot, J., et al. 2014b, A&A, 562, A124
McQuillan, A., Mazeh, T., & Aigrain, S. 2013, ApJ, 775, L11
McQuillan, A., Mazeh, T., & Aigrain, S. 2014, ApJS, 211, 24
Micela, G., Sciortino, S., Serio, S., et al. 1985, ApJ, 292, 172
Noyes, R. W., Hartmann, L. W., Baliunas, S. L., Duncan, D. K., & Vaughan, A. H. 1984, ApJ, 279, 763
O'dell, M. A., Panagi, P., Hendry, M. A., & Collier Cameron, A. 1995, A&A, 294, 715
Pandey, J. C., & Singh, K. P. 2012, MNRAS, 419, 1219
Pecaut, M. J., & Mamajek, E. E. 2013, ApJS, 208, 9
Pedersen, M. G., Antoci, V., & Korhonen, H. 2016, in Solar and Stellar Flares and their Effects on Planets, eds. A. G. Kosovichev, S. L. Hawley, & P. Heinzel, IAU Symp., 320, 150
Pinsonneault, M. H., An, D., Molenda-Żakowicz, J., et al. 2012, ApJS, 199, 30
Pizzolato, N., Maggio, A., Micela, G., Sciortino, S., & Ventura, P. 2003, A&A, 397, 147
Poretti, E. 1994, A&A, 285, 524
Rosen, S. R., Webb, N. A., Watson, M. G., et al. 2016, A&A, 590, A1
Scargle, J. D., Norris, J. P., Jackson, B., & Chiang, J. 2013, ApJ, 764, 167
Schmitt, J. H. M. M., & Liefke, C. 2004, A&A, 417, 651
Schröder, C., & Schmitt, J. H. M. M. 2007, A&A, 475, 677
Shkolnik, E. L. 2013, ApJ, 766, 9
Simon, T., Ayres, T. R., Redfield, S., & Linsky, J. L. 2002, ApJ, 579, 800
Skumanich, A. 1972, ApJ, 171, 565
Smith, R. K., Brickhouse, N. S., Liedahl, D. A., & Raymond, J. C. 2001, ApJ, 556, L91
Smith, K. L., Boyd, P. T., Mushotzky, R. F., et al. 2015, AJ, 150, 126
Stelzer, B., Marino, A., Micela, G., López-Santiago, J., & Liefke, C. 2013, MNRAS, 431, 2063
Stelzer, B., Damasso, M., Scholz, A., & Matt, S. P. 2016, MNRAS, 463, 1844
Vaníček, P. 1971, Ap&SS, 12, 10
Walter, F. M., & Bowyer, S. 1981, ApJ, 245, 671
Wenger, M., Ochsenbein, F., Egret, D., et al. 2000, A&AS, 143, 9
Wilson, O. C. 1966, ApJ, 144, 695
Wright, N. J., & Drake, J. J. 2016, Nature, 535, 526
Wright, N. J., Drake, J. J., Mamajek, E. E., & Henry, G. W. 2011, ApJ, 743, 48
Wright, N. J., Newton, E. R., Williams, P. K. G., Drake, J. J., & Yadav, R. K. 2018, MNRAS, 479, 2351
Zacharias, N., Finch, C. T., Girard, T. M., et al. 2012, VizieR Online Data Catalog: I/322
Zhao, G., Zhao, Y.-H., Chu, Y.-Q., Jing, Y.-P., & Deng, L.-C. 2012, Res. Astron. Astrophys., 12, 723

Appendix A: Additional tables

Table A.1. KIC (Brown et al. 2011) photometry all the 125 stars in the *Kepler*/*XMM-Newton* sample, with the corrections by Pinsonneault et al. (2012) for the SLOAN filters and updated magnitudes from the UCAC-4 Catalogue (Zacharias et al. 2012).

KIC ID	J (mag)	H (mag)	K_s (mag)	U (mag)	B (mag)	V (mag)	K_p (mag)	g_{SDSS} (mag)	r_{SDSS} (mag)	i_{SDSS} (mag)	z_{SDSS} (mag)	GALEX_FUV (mag)	GALEX_NUV (mag)
4 935 950	9.257	8.679	8.513	–	–	–	11.071	12.18	11.022	10.571	10.319	–	–
4 937 350	13.109	12.756	12.698	15.291	15.222	14.587	14.273	14.664	14.197	14.034	13.946	–	–
5 023 534	11.52	11.185	11.072	–	13.758	13.061	13.083	13.688	13.013	12.767	–	–	–
5 023 985	12.412	12.125	12.082	14.489	14.346	13.715	13.495	13.858	13.42	13.267	13.224	–	–
5 024 138	13.833	13.579	13.58	15.962	15.851	15.29	14.964	15.344	14.887	14.728	14.641	–	–
5 024 146	13.573	13.24	13.162	–	–	–	14.845	15.44	14.785	14.533	14.431	–	–
5 024 450	13.942	13.628	13.56	15.976	15.856	15.284	15.063	15.476	14.981	14.816	14.719	–	–
5 025 233	11.371	11.083	11.012	13.281	13.268	12.693	12.435	12.765	12.366	12.219	12.179	–	–
5 025 294	12.119	11.795	11.724	14.255	14.144	13.53	13.266	13.65	13.192	13.031	12.956	–	–
5 111 932	11.371	11.125	11.09	12.804	12.832	12.397	12.288	12.483	12.21	12.122	12.108	–	–
5 112 483	9.263	8.583	8.365	–	13.369	12.078	11.244	11.795	11.165	10.947	–	–	–
5 112 508	12.551	11.912	11.71	18.739	17.736	16.403	15.342	17.196	–	14.586	13.964	–	–
5 112 553	11.185	10.856	10.771	–	–	–	12.314	12.764	12.221	12.053	11.985	–	–
5 112 741	10.66	10.073	9.923	14.718	13.963	12.966	12.449	13.365	12.38	12.018	11.791	–	–
5 113 557	5.799	5.75	5.717	–	–	–	6.266	6.308	–	–	–	–	–
5 113 797	8.696	8.598	8.59	–	–	–	9.152	8.977	9.131	9.215	9.323	–	–
5 200 185	13.651	13.05	12.903	18.193	17.141	16.131	15.509	16.574	15.496	15.025	14.747	–	–
5 397 900	13.689	13.652	13.268	16.332	16.1	15.383	15.005	15.512	14.942	14.726	14.667	–	–
5 481 017	16.679	16.027	16.05	–	19.285	18.444	17.861	18.727	17.828	–	–	–	–
5 482 181	12.284	11.752	11.603	16.126	15.465	14.469	14.047	14.958	13.99	13.633	13.397	–	–
5 483 081	8.115	7.129	6.717	–	16.090	14.849	13.023	16.243	14.132	11.836	10.355	–	–
5 653 243	9.655	9.257	9.146	12.523	12.123	11.273	11.012	12.18	–	–	–	–	–
5 739 251	11.465	10.826	10.663	17.17	15.976	14.705	13.789	15.342	13.96	13.148	12.676	–	–
6 761 498	10.781	10.446	10.342	13.302	12.972	12.274	12.027	12.501	11.945	11.757	11.68	–	–
6 761 532	9.872	9.544	9.458	12.023	11.869	11.235	11.064	11.499	10.988	10.809	10.74	22.479	16.606
6 761 559	13.808	13.481	13.416	15.913	15.751	15.132	14.955	15.343	14.879	14.717	14.645	–	–
6 846 570	12.255	11.618	11.468	–	–	–	14.696	16.122	14.815	14.086	13.634	–	–
6 846 595	11.186	10.994	10.974	12.495	12.565	12.141	12.066	12.193	11.963	11.902	11.917	20.516	15.813
6 847 018	12.346	12.124	12.071	13.953	13.972	13.476	13.344	13.596	13.252	13.156	13.141	–	–
6 932 782	10.465	10.262	10.207	–	11.956	11.5	11.394	11.825	–	–	–	21.233	15.711
7 017 862	12.083	11.766	11.698	14.134	13.979	13.368	13.128	13.472	13.042	12.906	12.858	–	18.408
7 018 131	12.439	11.974	11.853	15.822	15.122	14.275	13.93	14.636	13.856	13.576	13.452	–	21.257
7 018 267	11.141	10.573	10.442	15.743	14.593	13.548	13.002	14.077	12.97	12.514	12.254	–	21.926
7 018 277	14.314	13.884	13.75	17.472	17.0	16.204	15.841	16.494	15.781	15.507	15.369	–	–
7 018 323	12.957	12.348	12.14	18.512	17.444	16.16	15.308	16.847	15.464	14.658	14.209	–	–
7 018 521	11.284	10.893	10.839	13.487	13.35	12.707	12.476	12.915	12.409	12.22	12.133	–	18.001
7 018 708	10.464	10.105	9.942	13.118	12.82	12.115	12.088	12.477	11.658	11.838	11.385	22.556	17.609
7 955 782	9.561	9.319	9.268	–	11.215	10.698	10.589	11.124	–	–	–	21.022	15.138
8 024 987	11.579	11.182	11.128	14.552	14.033	13.243	12.938	13.524	12.852	12.627	12.507	22.838	19.819
8 025 009	14.742	14.476	14.529	17.152	16.886	16.207	15.956	16.383	15.884	15.704	15.62	–	22.214
8 058 211	12.999	12.314	12.198	18.295	17.127	15.839	15.124	16.378	15.147	14.573	14.206	–	–
8 093 473	12.006	11.346	11.16	18.267	17.273	15.883	14.768	16.604	15.173	14.017	13.4	22.373	21.908
8 094 140	13.134	12.534	12.388	–	–	–	15.159	16.314	15.195	14.645	14.296	–	–
8 094 292	15.826	15.186	15.255	–	–	–	16.966	17.522	–	–	–	–	–
8 195 877	12.294	11.973	11.88	14.333	14.282	13.69	13.441	13.84	13.387	13.2	13.129	–	–
8 229 034	12.954	12.548	12.438	16.332	15.682	14.812	14.375	15.023	14.274	14.042	13.9	–	22.015
8 454 353	12.423	11.795	11.551	18.172	17.297	16.005	14.894	16.575	15.151	14.195	13.685	–	–
8 517 293	10.649	10.387	10.304	–	12.477	11.882	12.233	12.418	12.128	12.069	–	–	–
8 517 303	9.541	8.887	8.785	14.053	13.13	11.993	11.43	12.371	11.405	10.992	10.699	–	19.49
8 518 250	9.558	9.001	8.856	–	12.63	11.617	10.996	12.779	–	–	–	–	19.677
8 518 323	12.337	12.054	11.992	14.384	14.347	13.73	13.477	13.88	13.415	13.234	13.171	–	–
8 520 065	12.737	12.385	12.333	15.149	14.977	14.279	13.989	14.525	13.934	13.698	13.583	–	19.48
8 520 464	12.352	12.032	11.955	14.732	14.576	13.948	13.631	14.117	13.579	13.358	13.254	–	–
8 581 658	12.253	11.997	11.946	14.239	14.166	13.579	13.396	13.736	13.326	13.176	13.104	–	–
8 582 224	12.125	11.849	11.763	14.518	14.335	13.663	13.42	13.899	13.347	13.15	13.051	–	19.367
8 582 406	11.291	10.715	10.526	16.441	15.212	14.022	13.339	14.592	13.338	12.788	12.472	–	21.83

Table A.1. continued.

KIC ID	J (mag)	H (mag)	K_s (mag)	U (mag)	B (mag)	V (mag)	K_p (mag)	g_{SDSS} (mag)	r_{SDSS} (mag)	i_{SDSS} (mag)	z_{SDSS} (mag)	GALEX_FUV (mag)	GALEX_NUV (mag)
8 583 756	13.262	12.596	12.403	18.988	17.732	16.498	15.579	17.075	–	14.942	14.5	–	–
8 583 911	12.939	12.516	12.462	15.9	15.557	14.763	14.395	15.026	14.313	14.068	13.901	–	–
8 584 439	12.528	12.102	12.099	14.802	14.661	14.033	13.707	14.203	13.673	13.43	13.331	–	–
8 584 672	8.939	8.217	8.074	13.672	12.615	11.43	10.889	11.966	10.86	10.402	10.121	–	–
8 584 920	11.699	11.486	11.408	–	13.59	13.046	13.198	13.688	13.124	12.923	–	–	17.854
8 584 977	10.626	10.431	10.378	–	12.189	11.714	11.565	12.043	–	–	–	20.536	15.934
8 584 986	13.007	12.381	12.226	18.15	17.014	15.795	15.18	16.358	15.178	14.657	14.298	–	–
8 585 000	12.026	11.497	11.435	15.63	14.849	13.941	13.561	14.346	13.486	13.179	13.024	–	–
8 647 149	11.08	10.848	10.755	–	–	–	12.271	12.657	12.195	12.034	11.957	23.179	17.262
8 647 865	9.962	9.81	9.786	–	11.214	–	10.733	11.114	–	–	–	18.761	14.419
8 648 195	11.965	11.647	11.567	14.335	14.229	13.536	13.248	13.773	13.194	12.961	12.853	–	18.907
8 648 671	9.901	9.355	9.231	13.932	13.103	12.043	11.616	12.503	11.543	11.196	10.969	–	20.281
8 649 876	11.396	11.166	11.092	13.469	13.331	12.754	12.556	12.965	12.49	12.311	12.246	–	–
8 650 057	10.696	10.574	10.503	12.138	12.179	11.752	11.642	11.84	11.555	11.473	11.476	20.718	15.566
8 702 424	12.294	11.867	11.801	14.888	14.604	13.897	13.6	14.129	13.535	13.312	13.191	–	–
8 702 606	8.089	7.743	7.684	–	–	–	9.292	9.729	9.236	9.037	8.946	–	–
8 703 129	10.375	9.964	9.839	13.904	13.152	12.227	11.893	12.619	11.81	11.532	11.373	–	–
8 703 413	8.295	8.275	8.227	–	–	–	8.712	8.62	8.665	8.762	8.856	–	–
8 703 528	11.619	11.272	11.182	14.706	14.393	13.646	13.034	13.663	12.925	12.708	12.647	–	–
8 712 626	10.433	10.01	9.951	12.792	12.634	11.937	11.634	12.065	11.587	11.382	11.313	–	17.381
8 713 594	12.451	12.282	12.141	14.516	14.37	13.793	13.613	13.977	13.554	13.384	13.282	–	–
8 713 822	12.487	12.048	11.913	16.398	15.754	14.783	14.258	15.112	14.232	13.852	13.608	–	22.126
8 713 828	11.306	11.111	11.019	–	13.208	12.666	12.525	13.122	12.457	12.212	–	21.63	17.139
8 767 669	11.829	11.239	11.067	16.726	15.577	14.507	13.875	15.062	13.886	13.347	13.011	–	–
8 832 676	13.122	12.425	12.262	18.833	17.747	16.395	15.466	16.967	15.562	14.827	14.396	–	–
8 840 075	9.453	9.223	9.202	–	–	–	10.353	10.851	–	–	–	20.471	14.813
8 841 307	12.108	11.596	11.544	15.545	14.973	14.051	13.703	14.469	13.641	13.327	13.141	–	21.01
8 841 616	10.231	9.653	9.456	–	13.806	12.697	12.833	13.769	12.795	12.394	–	22.512	19.069
8 842 083	7.426	6.889	6.796	11.301	–	–	9.091	9.948	9.029	8.683	8.49	–	–
8 842 170	13.339	13.048	12.978	16.044	15.863	15.115	14.876	15.417	14.813	14.583	14.417	–	–
8 909 045	9.692	8.804	8.506	–	–	–	12.604	14.47	12.681	11.83	11.248	–	–
8 909 598	13.361	12.633	12.437	–	18.446	16.955	16.242	17.534	–	–	–	–	–
8 909 758	11.819	11.547	11.496	14.05	13.84	13.238	13.023	13.502	12.954	12.753	12.666	–	–
8 909 833	13.436	12.723	12.57	18.853	17.533	16.263	15.608	16.998	15.591	15.006	14.628	–	–
8 977 176	12.438	12.172	12.099	14.373	14.322	13.779	13.545	13.871	13.495	13.331	13.263	22.528	–
8 977 179	13.207	12.63	12.55	17.107	16.172	15.186	14.769	15.526	14.65	14.395	14.213	–	–
8 977 559	12.506	12.17	12.086	14.958	14.812	14.093	13.777	14.288	13.753	13.496	13.379	–	19.486
8 977 910	12.352	11.737	11.522	18.774	17.632	16.251	15.103	17.011	15.569	14.328	13.701	–	–
8 979 190	9.44	9.221	9.165	–	10.985	–	10.302	10.891	–	–	–	19.161	14.318
8 980 010	9.933	9.749	9.724	11.415	11.383	–	10.866	11.049	10.765	10.703	10.719	19.945	14.772
9 046 085	7.91	7.427	7.304	11.908	10.995	–	9.64	10.489	9.565	9.234	9.027	23.046	18.219
9 046 855	12.525	11.836	11.704	17.976	16.609	15.322	14.583	15.908	14.574	14.004	13.687	–	–
9 046 892	12.682	12.365	12.285	15.152	14.953	14.267	13.921	14.424	13.887	13.642	13.516	–	19.708
9 048 032	13.19	12.651	12.36	–	19.189	17.756	16.57	18.036	–	–	–	–	–
9 048 114	10.032	9.933	9.907	11.404	11.256	–	10.84	10.88	10.76	10.749	10.769	17.136	14.393
9 048 551	11.233	10.608	10.465	16.563	15.345	14.085	13.383	14.701	13.407	12.807	12.477	–	21.9
9 048 949	10.439	10.01	9.849	13.173	12.854	12.119	11.844	12.435	11.738	11.532	11.477	23.15	17.842
9 048 976	11.82	11.185	11.047	16.628	15.392	14.251	13.713	14.834	13.632	13.206	12.958	–	–
9 410 279	12.327	11.82	11.708	16.387	15.467	14.5	14.039	14.929	13.995	13.619	13.409	–	–
9 470 175	14.295	13.839	13.726	17.117	16.789	16.027	15.347	15.928	15.269	15.039	14.928	–	21.727
9 471 538	12.021	11.731	11.679	13.643	13.705	13.206	13.095	13.316	13.015	12.918	12.894	–	–
9 532 030	6.621	6.011	5.868	–	–	–	8.441	9.398	8.383	7.997	7.796	–	–
9 532 379	11.122	10.72	10.64	13.891	13.42	12.678	12.405	12.945	12.318	12.112	11.998	–	–
9 532 421	14.944	14.564	14.397	18.995	18.119	17.212	16.77	17.687	–	–	16.119	–	–
9 532 591	14.14	13.698	13.637	16.732	16.501	15.791	15.426	15.986	15.365	15.127	14.976	–	–
9 532 637	15.602	15.047	15.17	–	19.076	17.974	17.453	18.566	17.442	–	16.66	–	–
9 532 903	9.464	8.996	8.9	–	–	–	10.936	11.632	10.848	10.585	10.437	–	–
9 533 014	12.651	12.236	12.125	15.882	15.25	14.435	14.073	14.732	13.999	13.737	13.626	–	–
9 594 273	13.093	12.683	12.617	15.607	15.354	14.679	14.337	14.809	14.274	14.069	13.938	–	–

Table A.1. continued.

KIC ID	J (mag)	H (mag)	K_s (mag)	U (mag)	B (mag)	V (mag)	K_p (mag)	g_{SDSS} (mag)	r_{SDSS} (mag)	i_{SDSS} (mag)	z_{SDSS} (mag)	GALEX_FUV (mag)	GALEX_NUV (mag)
9 594 647	12.823	12.537	12.509	14.541	14.548	14.049	13.846	14.14	13.787	13.643	13.598	–	–
9 654 881	12.76	12.598	12.537	14.265	14.245	13.797	13.686	13.83	13.578	13.506	13.544	–	–
9 655 134	12.359	11.944	11.864	14.97	14.64	13.972	13.632	14.154	13.562	13.345	13.232	–	–
11 970 692	11.859	11.298	11.182	15.573	14.81	13.84	13.516	14.369	13.453	13.109	12.861	–	–
11 971 335	10.855	10.573	10.518	12.835	12.803	12.216	12.027	12.377	11.939	11.803	11.744	–	–
12 020 532	9.509	9.147	9.076	12.298	11.83	–	10.887	11.439	10.788	10.587	10.484	–	–
12 020 628	7.974	7.57	7.464	11.322	–	–	9.505	10.198	9.388	9.154	9.013	–	–
12 069 262	12.041	11.826	11.766	13.637	13.699	13.194	13.011	13.243	12.939	12.83	12.83	–	–
12 118 682	10.154	9.608	9.478	14.02	13.216	12.259	11.891	12.734	11.827	11.487	11.289	–	–
12 118 993	12.458	12.007	11.904	15.044	14.764	14.055	13.854	14.431	13.805	13.548	13.419	–	–

Table A.2. Fundamental stellar parameters for all 125 stars in the *Kepler*/*XMM-Newton* sample.

KIC ID	A_V (mag)	$\log g_\odot$	$[Fe/H]_\odot$	T_{eff} (K)	d (pc)	Flag d	M_* ($M_\odot$)	$\log L_{bol}$ ($L_\odot$)	SpT	Variability [(a)]	Flag
4 935 950	0.04	4.37	0.040	4381 ± 124	64.7 ± 6.1	Jmag	0.71 ± 0.04	−0.79 ± 0.11	K	ROT	
4 937 350	0.44	4.37	−0.24	6141 ± 186	1435.5 ± 38.3	*Gaia*	1.13 ± 0.13	0.22 ± 0.45	F	CONT?	
5 023 534	=0.38	4.15	−0.39	5842 ± 101	658.1 ± 22.7	Jmag	0.93 ± 0.00	0.50 ± 0.03	G	ROT	
5 023 985	0.39	4.27	0.079	6251 ± 185	625.3 ± 5.0	*Gaia*	1.18 ± 0.22	0.37 ± 0.47	F	ROT	
5 024 138	0.54	4.48	−1.90	6156 ± 204	774.4 ± 66.4	Jmag	0.75 ± 0.03	−0.21 ± 0.11	F	ROT	
5 024 146	0.57	4.24	−1.53	6121 ± 214	772.6 ± 98.8	Jmag	0.74 ± 0.03	−0.12 ± 0.14	F	ECL	
5 024 450	0.54	4.42	−0.06	6199 ± 216	2551.9 ± 145.3	*Gaia*	1.24 ± 0.15	0.36 ± 0.29	F	ECL	
5 025 233	0.25	4.30	−0.40	6103 ± 168	401.7 ± 183.5	Jmag	0.89 ± 0.13	0.18 ± 0.46	F	ROT	
5 025 294	0.26	4.49	−0.45	5933 ± 168	437.0 ± 39.2	Jmag	0.86 ± 0.05	−0.07 ± 0.10	G	ECL	
5 111 932	0.27	4.36	−0.41	6570 ± 182	440.1 ± 158.0	Jmag	1.05 ± 0.09	0.32 ± 0.44	F	ROT	
5 112 483	=0.38	4.68	−0.16	4086 ± 143	50.6 ± 5.1	Jmag	0.64 ± 0.04	−1.04 ± 0.11	K	ROT	
5 112 508	0.21	3.98	0.570	3656 ± 127	192.8 ± 22.9	Jmag	0.57 ± 0.05	−1.27 ± 0.15	M	ROT	DSEP out.
5 112 553	0.33	3.90	0.221	5941 ± 177	502.7 ± 110.8	Jmag	1.21 ± 0.09	0.40 ± 0.29	G	ROT	
5 112 741	0.61	2.67	−0.15	4752 ± 87	2932.0 ± 178.0	*Gaia*	1.91 ± 0.40	1.71 ± 0.28	K	ROT	
5 113 557	=0.38	4.11	−0.50	7082 ± 247	52.2 ± 21.4	Jmag	1.21 ± 0.28	0.76 ± 0.49	F	DSCU	
5 113 797	0.27	3.82	−0.27	8362 ± 292	384.4 ± 22.7	Jmag	1.76 ± 0.09	1.50 ± 0.08	A	GDOR?	
5 200 185	0.24	4.52	0.276	4525 ± 158	567.3 ± 29.9	Jmag	0.80 ± 0.03	−0.65 ± 0.07	K	ROT	
5 397 900	0.52	4.44	−0.26	5879 ± 190	1109.4 ± 30.6	*Gaia*	0.83 ± 0.08	−0.05 ± 0.12	G	ROT	
5 481 017	=0.38	=4.0	=0.0	5300 ± 200	6887.5 ± 210.0	Jmag	1.05 ± 0.00	0.40 ± 0.01	K	NOPER	VOSA, *
5 482 181	0.72	3.32	−0.06	5025 ± 175	2079.0 ± 1135.8	Jmag	1.63 ± 0.49	1.08 ± 0.55	K	ROT	
5 483 081	1.30	0.03	−0.06	5100 ± 200	446.8 ± 102.2	Jmag	2.11 ± 0.00	1.42 ± 0.23	K	NOPER	VOSA, DSEP out.
5 653 243	=0.38	3.56	−0.54	5190 ± 181	548.7 ± 8.8	*Gaia*	0.97 ± 0.46	0.67 ± 0.57	K	ROT	
5 739 251	0.06	4.64	0.221	3963 ± 138	137.4 ± 13.0	Jmag	0.63 ± 0.04	−1.07 ± 0.13	K	MULT	
6 761 498	0.21	4.30	0.020	5623 ± 123	223.3 ± 1.3	*Gaia*	0.94 ± 0.05	−0.01 ± 0.19	G	ROT	
6 761 532	0.25	4.25	0.030	5737 ± 91	215.6 ± 40.4	Jmag	0.99 ± 0.05	0.17 ± 0.17	G	ROT	
6 761 559	0.37	4.56	−0.28	6071 ± 178	1634.1 ± 58.7	*Gaia*	0.90 ± 0.04	0.01 ± 0.13	F	NOPER	
6 846 570	0.12	4.70	0.000	3834 ± 134	250.8 ± 1.4	*Gaia*	0.58 ± 0.06	−1.21 ± 0.17	M	ROT	
6 846 595	0.24	4.33	−0.22	6718 ± 184	468.1 ± 5.4	*Gaia*	1.40 ± 0.05	0.62 ± 0.07	F	ROT	
6 847 018	0.31	4.41	−0.03	6447 ± 184	677.2 ± 6.5	*Gaia*	1.40 ± 0.16	0.62 ± 0.26	F	ECL	
6 932 782	=0.38	4.07	−0.11	6329 ± 91	446.2 ± 72.4	Jmag	1.31 ± 0.09	0.65 ± 0.14	F	ROT	
7 017 862	0.22	4.16	0.140	5831 ± 73	652.9 ± 56.4	Jmag	1.08 ± 0.04	0.26 ± 0.14	G	ROT	
7 018 131	0.25	4.26	−0.12	5064 ± 145	356.2 ± 1.9	*Gaia*	0.84 ± 0.03	−0.42 ± 0.07	K	ROT	
7 018 267	0.10	4.32	0.407	4504 ± 129	170.6 ± 11.1	Jmag	0.78 ± 0.03	−0.70 ± 0.08	K	ROT	
7 018 277	0.37	4.51	−0.37	5248 ± 183	933.8 ± 28.4	*Gaia*	0.74 ± 0.03	−0.48 ± 0.10	K	ROT	
7 018 323	0.11	4.79	−0.10	3688 ± 129	199.9 ± 33.9	Jmag	0.52 ± 0.06	−1.38 ± 0.17	M	ROT	
7 018 521	0.13	4.17	0.080	5775 ± 98	410.2 ± 3.5	*Gaia*	1.02 ± 0.07	0.28 ± 0.18	G	ROT	
7 018 708	0.45	2.65	−0.12	5885 ± 583	1331.1 ± 83.6	Jmag	2.11 ± 0.00	1.53 ± 0.19	G	GDOR	
7 955 782	=0.38	4.20	0.000	6124 ± 214	226.2 ± 109.5	Jmag	1.15 ± 0.24	0.39 ± 0.48	F	ROT	

Notes. [(a)]The variability classification code (Col. 11) is the following: ROT: rotational variability; ROT UNCL: probably rotational variability but it is not possible to establish a reliable rotation period; UNCL: unclear periodic variability; NOPER: no apparent periodicity; ECL: eclipsing binary; CONT: contact binary; MULT: multiperiodic; DSCU: δ Scuti-like; GDOR: γ Dor-like.

Table A.2. continued.

KIC ID	A_V (mag)	$\log g_\odot$	$[Fe/H]_\odot$	T_{eff} (K)	d (pc)	Flag d	M_* ($M_\odot$	$\log L_{bol}$ ($L_\odot$)	SpT	Variability [a]	Flag
8 024 987	0.20	4.18	0.030	5469 ± 187	289.4 ± 1.9	*Gaia*	1.04 ± 0.01	0.40 ± 0.02	G	ROT	
8 025 009	0.47	4.68	−0.17	6086 ± 189	1801.4 ± 115.7	*Gaia*	1.12 ± 0.12	0.13 ± 0.22	F	ROT	
8 058 211	0.18	4.45	0.217	4257 ± 138	360.4 ± 18.9	Jmag	0.72 ± 0.04	−0.80 ± 0.12	K	ROT	
8 093 473	0.17	4.94	0.000	3354 ± 117	67.2 ± 25.0	Jmag	0.29 ± 0.14	−1.99 ± 0.34	M	ROT	
8 094 140	0.17	4.55	0.426	4432 ± 151	417.9 ± 21.3	Jmag	0.77 ± 0.03	−0.73 ± 0.08	K	ECL	
8 094 292	=0.38	=4.0	=0.0	5800 ± 200	4791.3 ± 3090.6	Jmag	1.11 ± 0.47	0.49 ± 0.55	G	NOPER	VOSA, *
8 195 877	0.40	4.16	−0.24	6256 ± 110	907.6 ± 11.8	*Gaia*	1.26 ± 0.09	0.52 ± 0.18	F	ECL	
8 229 034	0.45	3.91	0.282	5453 ± 190	1401.8 ± 34.5	*Gaia*	1.19 ± 0.01	0.48 ± 0.03	G	UNCL	
8 454 353	0.10	4.88	−0.10	3514 ± 122	132.1 ± 26.6	Jmag	0.47 ± 0.13	−1.54 ± 0.33	M	ROT	
8 517 293	=0.38	4.16	−0.05	5939 ± 107	277.4 ± 1.9	*Gaia*	1.09 ± 0.06	0.37 ± 0.16	G	ROT	
8 517 303	0.51	2.83	−0.08	4798 ± 149	1009.0 ± 354.9	Jmag	1.73 ± 0.67	1.53 ± 0.36	K	ROT	
8 518 250	=0.38	4.35	0.090	4948 ± 249	84.4 ± 0.2	*Gaia*	0.79 ± 0.05	−0.49 ± 0.15	K	ROT	
8 518 323	0.49	4.06	0.000	6261 ± 114	761.8 ± 8.2	*Gaia*	1.24 ± 0.16	0.61 ± 0.18	F	ROT	
8 520 065	0.60	4.13	−0.03	6049 ± 132	1048.9 ± 224.5	Jmag	1.14 ± 0.11	0.45 ± 0.19	F	ROT UN	
8 520 464	0.51	4.17	0.050	5866 ± 89	660.3 ± 7.1	*Gaia*	1.05 ± 0.06	0.32 ± 0.16	G	ROT	
8 581 658	0.40	4.19	−0.48	6230 ± 187	959.5 ± 13.9	*Gaia*	0.94 ± 0.22	0.34 ± 0.49	F	ECL	
8 582 224	0.21	4.23	0.030	5798 ± 86	467.1 ± 3.3	*Gaia*	1.01 ± 0.05	0.22 ± 0.15	G	ROT	
8 582 406	0.06	4.06	−0.11	4533 ± 267	166.7 ± 0.4	*Gaia*	0.72 ± 0.05	−0.73 ± 0.16	K	ROT	
8 583 756	0.20	4.77	−0.20	3737 ± 130	290.0 ± 2.6	*Gaia*	0.54 ± 0.06	−1.31 ± 0.18	M	ROT	
8 583 911	0.33	4.36	−0.34	5240 ± 151	948.5 ± 17.1	*Gaia*	0.74 ± 0.03	−0.48 ± 0.10	K	ROT	
8 584 439	0.47	4.02	−0.49	5813 ± 187	692.3 ± 8.3	*Gaia*	0.93 ± 0.01	0.50 ± 0.04	G	ROT	
8 584 672	0.57	1.97	−0.69	4448 ± 135	1940.8 ± 420.5	Jmag	1.19 ± 0.00	2.30 ± 0.18	K	NOPER	
8 584 920	=0.38	4.04	−0.04	6285 ± 103	544.1 ± 8.1	*Gaia*	1.28 ± 0.10	0.65 ± 0.16	F	ROT	
8 584 977	=0.38	3.92	−0.32	6421 ± 224	522.5 ± 329.4	Jmag	1.11 ± 0.41	0.75 ± 0.54	F	ROT	
8 584 986	1.06	2.20	−0.39	4650 ± 162	7377.9 ± 2712.7	Jmag	0.99 ± 0.92	1.86 ± 0.49	K	NOPER	
8 585 000	0.32	3.70	0.080	5002 ± 200	1000.9 ± 591.6	Jmag	1.15 ± 0.54	0.55 ± 0.63	K	ROT	
8 647 149	0.19	4.11	−0.08	6285 ± 117	555.7 ± 101.7	Jmag	1.28 ± 0.09	0.59 ± 0.16	F	MULT	
8 647 865	=0.38	4.06	0.020	6904 ± 241	422.0 ± 200.7	Jmag	1.54 ± 0.33	0.88 ± 0.48	F	ROT	
8 648 195	0.58	4.15	−0.14	6043 ± 132	1034.7 ± 14.0	*Gaia*	1.13 ± 0.09	0.42 ± 0.17	F	ROT	
8 648 671	0.63	2.81	0.006	4997 ± 158	1323.3 ± 36.7	*Gaia*	2.11 ± 0.00	1.53 ± 0.21	K	NOPER	
8 649 876	0.48	3.70	−0.03	6181 ± 191	1085.9 ± 700.8	Jmag	1.52 ± 0.57	1.03 ± 0.54	F	ROT	
8 650 057	0.28	4.12	−0.19	6413 ± 92	393.9 ± 4.0	*Gaia*	1.33 ± 0.09	0.63 ± 0.14	F	ROT	
8 702 424	0.23	4.29	0.130	5741 ± 93	631.4 ± 85.9	Jmag	1.03 ± 0.04	0.13 ± 0.14	G	ROT	
8 702 606	0.03	3.99	−0.04	5599 ± 183	128.5 ± 92.4	Jmag	1.05 ± 0.58	0.42 ± 0.61	G	ROT	
8 703 129	0.41	2.99	−0.05	4964 ± 155	698.2 ± 11.5	*Gaia*	2.04 ± 0.56	1.49 ± 0.45	K	ROT	
8 703 413	0.21	3.77	0.254	7936 ± 277	161.8 ± 0.0	Jmag	1.50 ± 0.00	0.68 ± 0.00	A	ROT	
8 703 528	0.42	3.70	0.245	5498 ± 211	559.0 ± 6.3	*Gaia*	1.47 ± 0.00	0.81 ± 0.06	G	CONT	
8 712 626	0.28	4.24	−0.03	5770 ± 89	286.2 ± 46.6	Jmag	1.00 ± 0.05	0.20 ± 0.15	G	ROT	
8 713 594	0.69	4.11	−0.11	6563 ± 125	1491.1 ± 40.9	*Gaia*	1.39 ± 0.09	0.69 ± 0.14	F	ROT	
8 713 822	0.67	3.38	−0.44	5028 ± 175	800.0 ± 14.9	*Gaia*	0.95 ± 0.01	1.09 ± 0.48	K	ROT	
8 713 828	=0.38	4.13	−0.19	6591 ± 122	1067.2 ± 33.4	*Gaia*	1.38 ± 0.09	0.68 ± 0.14	F	ROT	
8 767 669	0.12	4.39	0.312	4331 ± 137	229.7 ± 0.0	Jmag	0.77 ± 0.00	−0.72 ± 0.00	K	MULT	
8 832 676	0.24	4.77	−0.20	3737 ± 130	230.4 ± 31.6	Jmag	0.54 ± 0.06	−1.31 ± 0.18	M	ROT	
8 840 075	=0.38	4.28	−0.28	6421 ± 224	190.4 ± 84.0	Jmag	0.99 ± 0.15	0.34 ± 0.46	F	ROT	
8 841 307	0.52	3.76	0.040	5120 ± 227	492.0 ± 5.0	*Gaia*	1.20 ± 0.67	0.55 ± 0.65	K	ROT	
8 841 616	=0.38	4.69	−0.76	4462 ± 156	76.4 ± 6.3	Jmag	0.54 ± 0.03	−1.02 ± 0.11	K	ECL	
8 842 083	0.29	2.24	−0.19	4769 ± 135	42.2 ± 0.0	Jmag	0.91 ± 0.00	−0.32 ± 0.00	K	ROT	
8 842 170	0.68	3.90	−0.21	5831 ± 204	1369.2 ± 63.9	*Gaia*	1.21 ± 0.53	0.64 ± 0.56	G	CONT?	
8 909 045	0.90	1.09	−0.08	3800 ± 200	5142.4 ± 1062.5	Jmag	1.44 ± 0.42	2.77 ± 0.19	M	NODATA	VOSA
8 909 598	=0.38	=4.0	=0.0	3600 ± 200	219.9 ± 66.6	Jmag	0.49 ± 0.14	−1.47 ± 0.39	M	ROT	VOSA, *
8 909 758	0.51	4.01	−0.03	6299 ± 108	910.4 ± 24.9	*Gaia*	1.38 ± 0.13	0.72 ± 0.17	F	ROT	
8 909 833	0.21	4.73	−0.20	3903 ± 136	313.6 ± 43.0	Jmag	0.60 ± 0.05	−1.15 ± 0.17	K	MULT	
8 977 176	0.49	4.14	−0.22	6499 ± 114	975.6 ± 18.1	*Gaia*	1.35 ± 0.08	0.63 ± 0.14	F	MULT	
8 977 179	0.30	4.41	−0.03	4992 ± 152	586.0 ± 7.3	*Gaia*	0.82 ± 0.04	−0.49 ± 0.10	K	ROT	
8 977 559	0.63	3.68	−0.74	5941 ± 209	1573.8 ± 1015.6	Jmag	1.21 ± 0.57	0.89 ± 0.57	G	ROT	
8 977 910	0.18	5.01	0.000	3283 ± 114	61.2 ± 30.7	Jmag	0.23 ± 0.12	−2.22 ± 0.62	M	ROT	
8 979 190	=0.38	4.14	−0.25	6459 ± 67	227.7 ± 32.4	Jmag	1.03 ± 0.04	0.50 ± 0.13	F	ROT	
8 980 010	0.16	4.11	−0.07	6446 ± 71	344.8 ± 58.7	Jmag	1.35 ± 0.10	0.65 ± 0.15	F	ROT	
9 046 085	0.38	2.67	−0.16	4857 ± 140	595.7 ± 138.3	Jmag	2.12 ± 0.00	1.72 ± 0.19	K	NOPER	

Table A.2. continued.

KIC ID	A_V (mag)	$\log g_\odot$	$[Fe/H]_\odot$	T_{eff} [K]	d (pc)	Flag d	M_* ($M_\odot$)	$\log L_{bol}$ ($L_\odot$)	SpT	Variability [a]	Flag
9 046 855	0.13	4.47	−0.10	4133 ± 124	254.4 ± 1.3	*Gaia*	0.66 ± 0.04	−0.96 ± 0.13	K	ROT	
9 046 892	0.64	4.09	−0.12	6304 ± 110	838.9 ± 11.5	*Gaia*	1.27 ± 0.13	0.61 ± 0.17	F	ROT	
9 048 032	=0.38	=4.0	=0.0	3400 ± 200	134.3 ± 66.5	Jmag	0.34 ± 0.17	−1.86 ± 0.59	M	ROT	VOSA, *
9 048 114	0.41	3.84	−0.03	7759 ± 434	388.9 ± 0.0	Jmag	1.53 ± 0.00	0.82 ± 0.00	A	ROT	
9 048 551	0.08	4.00	−0.08	4351 ± 273	125.9 ± 0.3	*Gaia*	0.68 ± 0.06	−0.83 ± 0.19	K	ROT	
9 048 949	0.11	4.42	−0.13	5185 ± 161	164.1 ± 12.4	Jmag	0.86 ± 0.03	−0.36 ± 0.09	K	ROT	
9 048 976	0.12	4.37	−0.49	4258 ± 125	197.2 ± 0.7	*Gaia*	0.58 ± 0.02	−1.02 ± 0.07	K	ROT	
9 410 279	0.15	4.48	−0.65	4575 ± 132	247.5 ± 15.1	Jmag	0.63 ± 0.02	−0.82 ± 0.07	K	ROT	
9 470 175	0.42	4.50	−0.02	5552 ± 170	1232.7 ± 47.2	*Gaia*	0.94 ± 0.06	−0.16 ± 0.09	G	CONT	
9 471 538	0.38	4.18	−0.29	6627 ± 196	749.1 ± 11.7	*Gaia*	1.07 ± 0.23	0.52 ± 0.48	F	ROT	
9 532 030	0.01	2.52	−0.02	4454 ± 77	343.7 ± 62.7	Jmag	1.07 ± 0.00	1.72 ± 0.20	K	NOPER	
9 532 379	0.22	4.07	−0.20	5408 ± 151	582.3 ± 8.6	*Gaia*	1.04 ± 0.00	0.40 ± 0.00	G	ROT	
9 532 421	0.53	4.25	0.051	4884 ± 170	1112.3 ± 46.2	Jmag	0.80 ± 0.03	−0.54 ± 0.09	K	ECL	
9 532 591	0.39	4.58	−0.41	5502 ± 164	1574.4 ± 103.2	*Gaia*	0.77 ± 0.14	−0.35 ± 0.25	G	CONT?	
9 532 637	0.40	4.57	−0.16	4507 ± 157	1327.2 ± 152.4	Jmag	0.75 ± 0.05	−0.68 ± 0.14	K	ECL	
9 532 903	0.49	2.70	−0.09	4984 ± 94	977.2 ± 145.7	Jmag	2.11 ± 0.00	1.55 ± 0.12	K	ROT	
9 533 014	0.34	4.15	−0.02	5276 ± 158	523.1 ± 5.3	*Gaia*	1.05 ± 0.00	0.40 ± 0.01	K	ROT	
9 594 273	0.31	4.52	−0.61	5647 ± 168	854.9 ± 16.5	*Gaia*	0.78 ± 0.13	−0.23 ± 0.14	G	GDOR?	
9 594 647	0.34	4.50	−0.76	6296 ± 184	956.2 ± 17.3	*Gaia*	0.84 ± 0.04	0.02 ± 0.13	F	NOPER	
9 654 881	0.51	4.12	−0.16	7050 ± 227	1164.8 ± 29.9	*Gaia*	1.53 ± 0.32	0.84 ± 0.48	F	UNCL	
9 655 134	0.23	4.46	−0.66	5389 ± 153	463.9 ± 4.4	*Gaia*	0.77 ± 0.03	−0.38 ± 0.10	G	ROT	
11 970 692	0.49	3.19	−0.24	4887 ± 145	1315.6 ± 26.7	*Gaia*	1.44 ± 0.67	1.12 ± 0.56	K	ROT	
11 971 335	0.16	4.48	−0.33	5912 ± 161	244.2 ± 17.7	Jmag	0.85 ± 0.06	−0.08 ± 0.07	G	ROT	
12 020 532	0.25	2.66	−0.18	5036 ± 211	920.3 ± 265.1	Jmag	2.11 ± 0.00	1.49 ± 0.27	K	ROT UN	
12 020 628	0.34	2.87	0.268	5239 ± 166	366.7 ± 0.7	Jmag	2.18 ± 0.00	1.32 ± 0.05	K	ROT	
12 069 262	0.37	4.16	−0.19	6589 ± 194	871.3 ± 342.4	Jmag	1.35 ± 0.27	0.63 ± 0.48	F	ROT	
12 118 682	0.46	2.66	−0.20	4918 ± 146	1754.4 ± 73.3	*Gaia*	2.11 ± 0.00	1.64 ± 0.19	K	ROT	
12 118 993	0.21	4.55	−0.92	5180 ± 151	842.4 ± 12.0	*Gaia*	0.65 ± 0.02	−0.63 ± 0.07	K	ROT	

Table A.3. Rotation and flaring parameters derived from the *Kepler* light curves for all 74 rotationally-variable main-sequence stars in the *Kepler*/*XMM-Newton* sample.

KIC ID	P_{rot} (d) (1)	R_0 (2)	$\log R_{per}$ (%) (3)	S_{ph} (ppm) (4)	$S_{ph,5}$ (ppm) (5)	S_{flat} (ppm) (6)	$\langle \log A_{peak} \rangle$ (7)	$\log A_{peak,min}$ (8)	$\log A_{peak,max}$ (9)	Flare rate (d^{-1}) (10)
4 935 950	12.66	0.38	−0.15	2621	2467	41.9	−3.28	−3.56	−2.34	0.012
5 023 534	17.76	1.52	−0.16	2361	2393	109.4	−2.94	−3.17	−2.48	0.015
5 023 985	6.58	1.40	0.16	5004	4911	142.0	−2.82	−2.83	−2.46	0.003
5 024 138	7.52	1.20	−0.83	471	467	326.4	–	–	–	–
5 025 233	4.04	0.56	−0.11	2866	2799	93.4	−2.83	−3.33	−2.01	0.060
5 111 932	1.45	1.56	−0.78	565	542	79.0	−3.07	−3.34	−2.79	0.015
5 112 483	63.51	1.64	0.54	9582	0	55.2	−3.25	−3.58	−2.93	0.006
5 112 508	0.76	0.02	0.41	8858	8309	1021.9	−1.49	−2.17	−1.09	0.098
5 112 553	5.33	0.53	−0.07	3285	3293	77.2	−3.10	−3.48	−2.46	0.010
5 200 185	3.74	0.12	0.49	11 797	11 809	519.4	−2.05	−2.50	−1.23	0.052
5 397 900	2.21	0.20	0.59	15 368	13 912	515.9	−2.11	−2.53	−1.58	0.053
5 653 243	19.66	0.92	0.27	6196	6196	80.5	−3.27	−3.31	−3.11	0.003
6 761 498	7.17	0.47	0.15	5160	4612	75.4	−3.11	−3.53	−2.36	0.017
6 761 532	4.82	0.36	0.45	9436	9127	69.5	−2.82	−3.22	−2.58	0.021
6 846 570	4.13	0.09	0.73	18 594	18 157	496.2	−2.05	−2.55	−0.72	0.183
6 846 595	1.00	3.90	−0.56	927	893	81.2	−2.74	−3.36	−2.49	0.025
6 932 782	12.87	3.67	−1.25	187	171	59.0	–	–	–	–

Notes. (1) Rotation period from ACF, (2) Rossby number from Eq. (36) in Cranmer & Saar (2011), (3) percentile amplitude of the rotation cycle after McQuillan et al. (2013), (4) standard deviation of the whole lightcurve, (5) average of the standard deviation for 5 rotation cycles after Mathur et al. (2014a), (6) minimum of the standard deviations from all quarters for the "flattened" lightcurves, (7) median of relative flare peak amplitudes, (8) minimum relative flare peak amplitude, (9) maximum relative flare amplitude, (10) flare rate.

Table A.3. continued.

KIC ID	$P_{\rm rot}$ (d) (1)	R_0 (2)	$\log R_{\rm per}$ (%) (3)	$S_{\rm ph}$ (ppm) (4)	$S_{\rm ph,5}$ (ppm) (5)	$S_{\rm flat}$ (ppm) (6)	$\langle \log A_{\rm peak} \rangle$ (7)	$\log A_{\rm peak,min}$ (8)	$\log A_{\rm peak,max}$ (9)	Flare rate (d^{-1}) (10)
7 017 862	2.02	0.17	−0.08	3734	3147	128.6	−2.68	−3.27	−1.80	0.066
7 018 131	10.59	0.46	0.16	4910	4454	164.5	−2.81	−2.89	−2.67	0.005
7 018 267	17.59	0.56	−0.19	2111	1986	103.7	–	–	–	–
7 018 277	1.57	0.08	0.62	16 197	15 241	648.3	−1.81	−2.62	−0.55	0.078
7 018 323	6.27	0.13	0.36	8191	7625	533.2	−2.12	−2.49	−0.90	0.052
7 018 521	10.79	0.84	−0.09	2832	2650	73.6	–	–	–	–
7 955 782	2.81	0.41	−0.26	2105	1973	43.2	−3.35	−3.61	−3.01	0.009
8 024 987	8.03	0.46	0.11	4804	4320	102.9	−2.93	−3.10	−2.81	0.001
8 025 009	13.97	1.87	−0.64	708	709	582.2	−1.51	−1.51	−1.51	0.001
8 058 211	1.70	0.05	0.69	16 504	16 518	623.2	−2.03	−2.66	−0.78	0.096
8 093 473	6.03	0.11	0.69	16 562	16 498	776.9	−1.79	−2.29	−0.56	0.228
8 454 353	1.49	0.03	0.58	14 157	13 433	640.0	−1.95	−2.69	−0.36	0.211
8 517 293	2.66	0.26	0.22	6293	5865	114.2	−2.68	−3.19	−2.18	0.011
8 518 250	19.62	0.80	0.21	6132	5911	60.7	−3.26	−3.43	−2.76	0.021
8 518 323	2.78	0.61	−0.23	2049	1906	155.1	−2.90	−2.91	−2.86	0.002
8 520 464	7.70	0.68	0.15	4680	4634	177.0	−2.80	−2.87	−2.68	0.002
8 582 224	8.99	0.72	0.14	4944	4815	157.4	−2.72	−2.82	−2.71	0.002
8 582 406	16.04	0.52	−0.22	2187	2069	155.5	–	–	–	–
8 583 756	9.24	0.20	0.46	10 156	9959	614.8	−2.25	−2.43	−2.02	0.009
8 583 911	4.21	0.20	0.16	5341	5385	264.9	−2.63	−2.72	−2.04	0.004
8 584 439	2.86	0.23	−0.06	3033	2914	186.8	−2.61	−2.86	−2.15	0.013
8 584 920	4.45	1.07	−0.54	1046	1005	109.8	–	–	–	–
8 584 977	2.15	0.93	−1.10	260	258	87.1	–	–	–	–
8 585 000	11.63	0.49	0.17	5397	4924	153.6	−2.79	−2.93	−2.56	0.013
8 647 865	1.25	–	−1.38	151	142	44.8	−3.34	−3.34	−3.34	0.001
8 648 195	7.36	0.89	−0.11	2832	2810	137.6	−2.71	−2.71	−2.71	0.001
8 649 876	10.81	1.85	−1.05	278	275	91.3	–	–	–	–
8 650 057	2.66	1.11	−1.13	247	240	60.8	−3.35	−3.35	−3.35	0.001
8 702 424	0.90	0.07	−0.31	1784	1631	147.6	−2.54	−3.14	−1.44	0.056
8 702 606	19.86	1.28	−1.48	98	98	63.1	–	–	–	–
8 703 413	6.62	–	−1.13	247	248	12.7	−3.97	−4.37	−3.73	0.002
8 712 626	9.99	0.77	−0.11	3168	3100	72.5	−3.25	−3.27	−2.72	0.002
8 713 594	2.49	2.55	−0.15	2280	2261	166.8	−2.85	−3.27	−2.58	0.008
8 713 828	2.57	3.23	−1.19	222	208	89.2	−3.06	−3.06	−3.06	0.001
8 832 676	10.93	0.24	0.10	4447	4310	541.9	−1.90	−2.51	−0.61	0.116
8 840 075	2.64	1.14	−1.34	198	181	35.9	−3.28	−3.28	−3.28	0.001
8 841 307	6.15	0.28	0.52	12 138	11 358	191.2	−2.65	−3.08	−2.10	0.018
8 909 758	3.09	0.78	−0.77	591	566	124.9	−2.91	−3.12	−2.46	0.008
8 977 179	1.59	0.07	−0.08	4048	3251	387.7	−2.29	−2.81	−1.97	0.011
8 977 559	2.47	0.25	−0.22	2244	2081	192.4	−2.64	−2.83	−1.92	0.004
8 977 910	10.73	0.18	0.33	7428	7109	528.5	−2.00	−2.47	−0.46	0.090
8 979 190	3.47	1.84	−1.24	214	211	40.7	–	–	–	–
8 980 010	2.27	1.12	−1.15	253	256	53.4	–	–	–	–
9 046 855	26.47	0.70	−0.07	2724	0	305.6	−2.66	−2.66	−2.66	0.001
9 046 892	6.54	1.69	−1.10	246	246	190.6	–	–	–	–
9 048 114	2.80	–	−0.92	446	422	36.2	−3.44	−3.44	−3.44	0.001
9 048 551	8.58	0.25	0.59	14 329	12 329	226.0	−2.49	−2.92	−1.47	0.164
9 048 949	3.47	0.16	0.57	14 386	13 203	192.0	−2.31	−2.95	−1.27	0.141
9 048 976	10.95	0.31	0.37	8089	7778	198.4	−2.43	−2.91	−1.57	0.097
9 410 279	1.57	0.05	−0.75	585	574	175.4	−2.61	−2.96	−1.84	0.032
9 471 538	0.90	1.50	−0.85	505	502	109.6	−2.75	−3.25	−1.41	0.047
9 532 379	9.26	0.51	0.38	9012	8354	94.9	−2.94	−2.94	−2.94	0.001
9 533 014	6.77	0.34	0.44	9615	9047	190.9	−2.59	−2.99	−2.34	0.006
9 655 134	15.09	0.81	−0.02	3539	2945	146.9	−2.59	−3.26	−1.27	0.044
11 971 335	0.78	0.07	0.66	16 547	15 162	985.7	−1.90	−2.02	−1.34	0.003
12 069 262	2.78	3.44	−0.23	2109	2010	126.3	−2.83	−3.13	−2.40	0.006
12 118 993	0.55	0.03	0.91	27 536	26 132	4247.5	−0.99	−1.23	−0.77	0.009

Table A.4. X-ray luminosity (in the 0.2–2 keV energy band), observed NUV and FUV luminosity, and NUV and FUV chromospheric excess luminosity.

KIC_ID	L_X (10^{29} erg s^{-1})	L_{NUV} (10^{29} erg s^{-1})	L_{FUV} (10^{29} erg s^{-1})	$L_{NUV,exc}$ (10^{29} erg s^{-1})	$L_{FUV,exc}$ (10^{29} erg s^{-1})
4 935 950	0.04 ± 0.02	–	–	–	–
4 937 350	21.40 ± 9.08	–	–	–	–
5 023 534	2.58 ± 1.34	896.0 ± 63.3	–	406.0	–
5 023 985	1.96 ± 0.99	490.0 ± 13.4	–	–	–
5 024 138	2.52 ± 1.29	–	–	–	–
5 024 146	4.51 ± 1.91	175.0 ± 47.6	–	–	–
5 024 450	40.05 ± 15.43	–	–	–	–
5 025 233	4.07 ± 3.91	674.0 ± 615.0	–	–	–
5 025 294	0.76 ± 0.36	–	–	–	–
5 111 932	1.23 ± 0.98	2480.0 ± 1780.0	–	–	–
5 112 483	0.04 ± 0.01	1.6 ± 0.3	–	1.5	–
5 112 508	1.71 ± 0.44	–	–	–	–
5 112 553	2.69 ± 1.32	692.0 ± 305.0	–	–	–
5 112 741	97.25 ± 28.24	–	–	–	–
5 113 557	0.89 ± 0.73	–	–	–	–
5 113 797	15.36 ± 2.94	–	–	–	–
5 200 185	4.12 ± 2.08	–	–	–	–
5 397 900	9.85 ± 5.35	2520.0 ± 155.0	–	–	–
5 481 017	840.55 ± 467.82	–	–	–	–
5 482 181	132.70 ± 147.01	1060.0 ± 1180.0	–	714.0	–
5 483 081	0.03 ± 0.48	–	–	–	–
5 653 243	18.36 ± 2.54	1100.0 ± 38.2	–	221.0	–
5 739 251	0.72 ± 0.17	–	–	–	–
6 761 498	0.72 ± 0.26	–	–	–	–
6 761 532	2.13 ± 0.86	393.0 ± 147.0	1.3 ± 0.6	–	1.0
6 761 559	36.58 ± 13.15	–	–	–	–
6 846 570	3.42 ± 0.58	–	–	–	–
6 846 595	2.28 ± 0.97	3700.0 ± 86.3	36.1 ± 4.2	–	–
6 847 018	2.67 ± 1.45	1490.0 ± 32.5	–	475.0	–
6 932 782	0.86 ± 0.52	5330.0 ± 1730.0	23.5 ± 8.0	–	–
7 017 862	10.88 ± 3.62	620.0 ± 107.0	–	–	–
7 018 131	0.54 ± 0.22	14.6 ± 0.2	–	7.8	–
7 018 267	0.08 ± 0.04	1.2 ± 0.2	–	1.0	–
7 018 277	10.62 ± 2.59	65.0 ± 11.4	–	45.3	–
7 018 323	0.39 ± 0.16	–	–	–	–
7 018 521	0.54 ± 0.26	284.0 ± 5.2	–	–	–
7 018 708	850.95 ± 112.24	10 200.0 ± 1280.0	74.6 ± 18.3	7190.0	73.8
7 955 782	3.66 ± 3.59	2320.0 ± 2250.0	7.3 ± 7.1	–	–
8 024 987	0.44 ± 0.20	31.9 ± 0.8	1.5 ± 0.5	14.1	1.5
8 025 009	20.11 ± 9.52	280.0 ± 47.6	–	–	–
8 058 211	3.23 ± 0.89	–	–	–	–
8 093 473	0.31 ± 0.27	0.2 ± 0.2	0.1 ± 0.1	0.2	0.1
8 094 140	2.72 ± 0.56	–	–	–	–
8 094 292	478.63 ± 648.79	–	–	–	–
8 195 877	32.17 ± 8.51	2040.0 ± 59.1	–	1140.0	–
8 229 034	30.87 ± 13.22	192.0 ± 21.1	–	85.1	–
8 454 353	1.04 ± 0.43	–	–	–	–
8 517 293	1.75 ± 0.39	647.0 ± 9.5	–	305.0	–
8 517 303	107.35 ± 75.72	1210.0 ± 852.0	–	1110.0	–
8 518 250	0.21 ± 0.02	4.9 ± 0.1	–	–	–
8 518 323	1.83 ± 0.54	1460.0 ± 41.4	–	554.0	–
8 520 065	54.89 ± 23.92	1670.0 ± 774.0	–	995.0	–
8 520 464	1.21 ± 0.46	–	–	–	–
8 581 658	4.59 ± 2.58	3310.0 ± 104.0	–	1310.0	–
8 582 224	0.37 ± 0.16	129.0 ± 2.7	–	–	–
8 582 406	0.06 ± 0.02	1.1 ± 0.0	–	1.0	–
8 583 756	0.59 ± 0.12	–	–	–	–

Table A.4. continued.

KIC_ID	L_X (10^{29} erg s^{-1})	L_{NUV} (10^{29} erg s^{-1})	L_{FUV} (10^{29} erg s^{-1})	$L_{NUV,exc}$ (10^{29} erg s^{-1})	$L_{FUV,exc}$ (10^{29} erg s^{-1})
8 583 911	3.37 ± 1.42	–	–	–	–
8 584 439	1.90 ± 0.50	862.0 ± 24.6	–	454.0	–
8 584 672	19.76 ± 9.77	–	–	–	–
8 584 920	0.60 ± 0.24	1100.0 ± 33.3	–	472.0	–
8 584 977	1.00 ± 1.28	5950.0 ± 7500.0	61.2 ± 77.2	–	20.0
8 584 986	117.23 ± 139.06	–	–	–	–
8 585 000	8.44 ± 10.25	134.0 ± 159.0	–	67.8	–
8 647 149	0.97 ± 0.46	1210.0 ± 443.0	3.9 ± 1.9	–	2.3
8 647 865	1.85 ± 1.77	15 700.0 ± 14 900.0	205.0 ± 195.0	4880.0	72.6
8 648 195	4.87 ± 1.20	2650.0 ± 77.3	–	1060.0	–
8 648 671	13.10 ± 6.69	1370.0 ± 469.0	–	813.0	–
8 649 876	4.45 ± 6.11	5220.0 ± 6740.0	–	–	–
8 650 057	0.36 ± 0.12	3680.0 ± 95.3	23.4 ± 0.5	–	–
8 702 424	8.31 ± 5.12	–	–	–	–
8 702 606	0.09 ± 0.14	–	–	–	–
8 703 129	3.61 ± 1.29	–	–	–	–
8 703 413	0.38 ± 0.10	–	–	–	–
8 703 528	17.32 ± 1.85	377.0 ± 8.6	–	233.0	–
8 712 626	0.78 ± 0.31	364.0 ± 119.0	–	–	–
8 713 594	6.58 ± 3.10	10 500.0 ± 587.0	–	3440.0	–
8 713 822	31.57 ± 3.04	102.0 ± 10.3	–	68.1	–
8 713 828	6.12 ± 2.38	8180.0 ± 588.0	93.2 ± 5.8	5280.0	90.3
8 767 669	0.79 ± 0.52	–	–	–	–
8 832 676	0.43 ± 0.24	–	–	–	–
8 840 075	0.32 ± 0.29	2220.0 ± 1960.0	8.6 ± 7.6	–	–
8 841 307	3.82 ± 0.46	72.0 ± 3.7	–	41.9	–
8 841 616	0.03 ± 0.01	7.1 ± 1.2	0.2 ± 0.1	6.9	0.2
8 842 083	0.09 ± 0.01	–	–	–	–
8 842 170	19.55 ± 5.02	1510.0 ± 150.0	–	1040.0	–
8 909 045	29.60 ± 26.21	–	–	–	–
8 909 598	0.41 ± 0.27	–	–	–	–
8 909 758	7.79 ± 2.72	2210.0 ± 123.0	–	543.0	–
8 909 833	0.69 ± 0.25	–	–	–	–
8 977 176	4.65 ± 1.06	–	44.6 ± 15.8	–	32.5
8 977 179	2.05 ± 0.47	–	–	–	–
8 977 559	12.63 ± 16.56	4050.0 ± 5220.0	–	–	–
8 977 910	0.06 ± 0.06	–	–	–	–
8 979 190	0.28 ± 0.12	5010.0 ± 1420.0	41.2 ± 11.8	2500.0	29.3
8 980 010	0.93 ± 0.37	4220.0 ± 1440.0	27.3 ± 9.4	–	–
9 046 085	1.62 ± 1.00	960.0 ± 446.0	8.0 ± 4.6	466.0	8.0
9 046 855	0.14 ± 0.07	–	–	–	–
9 046 892	3.55 ± 1.15	973.0 ± 31.6	–	113.0	–
9 048 032	1.19 ± 1.19	–	–	–	–
9 048 114	1.30 ± 0.37	15 100.0 ± 16.4	849.0 ± 5.6	2490.0	564.0
9 048 551	1.13 ± 0.06	0.6 ± 0.1	–	0.6	–
9 048 949	4.66 ± 0.79	49.0 ± 7.4	0.3 ± 0.1	28.4	0.3
9 048 976	0.70 ± 0.09	–	–	–	–
9 410 279	0.78 ± 0.43	–	–	–	–
9 470 175	17.29 ± 8.44	180.0 ± 21.4	–	101.0	–
9 471 538	10.19 ± 2.28	3040.0 ± 104.0	–	–	–
9 532 030	0.51 ± 0.25	92 200.0 ± 33 800.0	–	–	–
9 532 379	3.55 ± 0.87	326.0 ± 13.6	–	157.0	–
9 532 421	5.30 ± 2.80	–	–	–	–
9 532 591	10.62 ± 5.39	207.0 ± 54.1	–	–	–
9 532 637	6.51 ± 3.92	–	–	–	–
9 532 903	5.06 ± 2.85	–	–	–	–
9 533 014	1.97 ± 0.95	39.1 ± 9.3	–	20.7	–
9 594 273	4.98 ± 1.69	208.0 ± 18.7	–	51.5	–

Table A.4. continued.

KIC_ID	L_X (10^{29} erg s^{-1})	L_{NUV} (10^{29} erg s^{-1})	L_{FUV} (10^{29} erg s^{-1})	$L_{NUV,exc}$ (10^{29} erg s^{-1})	$L_{FUV,exc}$ (10^{29} erg s^{-1})
9 594 647	5.56 ± 4.52	–	–	–	–
9 654 881	32.92 ± 12.78	9880.0 ± 526.0	–	3620.0	–
9 655 134	3.88 ± 1.79	–	–	–	–
11 970 692	113.75 ± 27.30	–	–	–	–
11 971 335	23.96 ± 3.91	–	–	–	–
12 020 532	10.54 ± 7.22	–	–	–	–
12 020 628	5.09 ± 1.01	–	–	–	–
12 069 262	7.16 ± 6.39	–	–	–	–
12 118 682	69.36 ± 24.01	–	–	–	–
12 118 993	45.21 ± 9.50	318.0 ± 12.4	–	158.0	–